

CHALMERS



Design of Contraction, Test Section, and Diffuser for a High-Speed Water Tunnel

Master's thesis in Fluid Mechanics

IVAYLO NEDYALKOV

Department of Applied Mechanics
Division of Fluid Mechanics
CHALMERS UNIVERSITY OF TECHNOLOGY
Gothenburg, Sweden 2012
Master's thesis 2012:40

MASTER'S THESIS IN FLUID MECHANICS

Design of Contraction, Test Section, and Diffuser for a High-Speed
Water Tunnel

IVAYLO NEDYALKOV

Department of Applied Mechanics
Division of Fluid Mechanics
CHALMERS UNIVERSITY OF TECHNOLOGY
Gothenburg, Sweden 2012

Design of Contraction, Test Section, and Diffuser for a High-Speed Water Tunnel
IVAYLO NEDYALKOV

© IVAYLO NEDYALKOV, 2012

Master's thesis 2012:40
ISSN 1652-8557
Department of Applied Mechanics
Division of Fluid Mechanics
Chalmers University of Technology
SE-412 96 Gothenburg
Sweden
Telephone: +46 (0)31-772 1000

Cover:
Cavitating hydrofoil in the completed high-speed water tunnel (now called HiCAT)

Chalmers Reproservice
Gothenburg, Sweden 2012

Design of Contraction, Test Section, and Diffuser for a High-Speed Water Tunnel
Master's thesis in Fluid Mechanics
IVAYLO NEDYALKOV
Department of Applied Mechanics
Division of Fluid Mechanics
Chalmers University of Technology

ABSTRACT

Contraction, test section and diffuser for a high-speed water tunnel were designed. Theoretical and numerical studies were used to determine the components shapes and sizes, by investigating flow uniformity, flow speed and cavitation numbers, boundary layer growth and blockage ratio.

The design, which was limited by the rest of the water tunnel circuit, consisted of a 5th-order-polynomial-shaped contraction with contraction ratio of 7 and L/D ratio of 1.5; 6'' × 6'' × 36'' square test section, and a square-to-round transition/diffuser with a constant increase of cross-sectional area in downstream direction.

The components were designed, manufactured and installed. Further upgrades and modifications to the water tunnel were made, including installing a new motor and drive, new supports, and a shortened straight duct, which simplified installation. Additionally, a pressure/vacuum system was designed and installed to control test section pressure independently.

PTV, LDV, PIV and pressure measurements were performed for motor speeds between 10% and 76% of the maximum motor speed. The flow speed in the test section varied linearly as a function of the motor rpm, as anticipated, and its magnitude was larger than the originally expected. The growth of the boundary layer and resultant increase in center-line velocity were observed.

Suggestions were made for improving similar future work.

Keywords: Water tunnel, Contraction, Test section, Diffuser, PTV, LDV, PIV, Pressure measurements

Dedicated to my grandfather, who strived to serve as an example to others, in the 92 years of his life, and encouraged me to do likewise.

PREFACE

The work for this report was performed at the Center for Ocean Renewable Energy, Department of Mechanical Engineering at the University of New Hampshire under the supervision of Prof. Martin Wosnik from the Department of Mechanical Engineering at the University of New Hampshire and Prof. Gunnar Johansson from the Department of Applied Mechanics at Chalmers University of Technology.

ACKNOWLEDGEMENTS

I would like to thank my family, especially my mother and father, who have raised me in a good way, not only giving me advice and support, but also respecting my own opinion, thoughts and choices.

A big part of what I am, I owe to teachers and professors. There are many names to be mentioned here, but I would especially like to thank Prof. Vladimir Georgiev, without whom I might have not enrolled in Chalmers University of Technology.

A big thank you goes to the Swedish Embassy in Bulgaria, H.E. Bertil Roth, and the companies SAAB and Ericsson Telecom. Thanks to all of them, I had the chance to get acquainted with the wonderful Kingdom of Sweden, fall in love with it, and continue my education there.

I would also like to thank Prof. Lars Davidson (Lars), through whom I learned about the Applied Mechanics program and who explained fluid mechanics in a very understandable way, and Prof. William K. George (Bill) who not only taught me a lot about Turbulence, but also helped me to find a good university for my doctorate studies. I am thankful to Prof. Gunnar Johansson (Gunnar) who agreed to be my advisor and provided me with excellent feedback, and to Prof. Martin Wosnik (Martin) who supervised me in my work, gave me valuable advice, and certainly helped me the most. I would like to thank prof. Jim Forsythe for providing additional CFD analysis and William Hambleton for the help and discussions at the early stage of the test section design.

I want to thank my friend Faraz Mehdi, who made my time at the University of New Hampshire much better, in many aspects - I couldn't have asked for a better officemate. I am also very grateful to Peter Bachant, from whom I learned a lot, and who has helped me, especially in the detailed component design and refining drawings for the water tunnel components. I am very thankful to the UNH undergraduate students Ben Comtois, Ryan Therrien and Spencer Roux for the enormous help in assembling the water tunnel.

I would like to thank all my other friends, and especially my closest ones. They have always supported me in hard times, made me laugh for hours, encouraged me to accomplish my goals, and helped me to realize that I should value all my resources (especially time), and use them wisely. A special thank you to Ivo, Kriss, and Diana!

Last but not least, I would like to thank my girlfriend Rebecca, who constantly inspires and motivates me.

(Ivaylo Nedyalkov)
(2012)

NOMENCLATURE

Upper-case Roman

A	cross sectional area
A_{CI}	cross sectional area at the contraction inlet
A_{CO}	cross sectional area at the contraction outlet
A_{DI}	cross sectional area at the diffuser inlet
A_{DO}	cross sectional area at the diffuser outlet
A_W	window area
A_f	shear area of fasteners
A_g	O-ring groove cross sectional area
A_o	O-ring cross sectional area
$A_{t,sa}$	total shear area
A_w	throat area of the weld
AR	area ratio
AR_d	desired area ratio
B	blockage ratio
C_1, C_2	coefficients for equations 4.5 and 4.6
D	diameter
D_2	diameter of inlet of existing diffuser (part # 2)
D_w	weld size (in inches)
E	Young's modulus
F	force
F_{EXX}	constant used in equation 4.15
F_a	axial force
F_p	force due to pressure difference
F_{px}	force due to pressure difference, acting in horizontal direction.
F_w	force on weld
FS_f	factor of safety for fasteners
FS_w	factor of safety for windows
L/D	length/diameter ratio
L_1, L_2	width and length of the windows
L_C	length of contraction
L_D	length of diffuser
L_{TS}	length of test section
M	average honeycomb cell size
M_h	average honeycomb cell height
M_w	average honeycomb cell width
$(M_x)_{max}$	maximum bending moment per unit length
N_f	number of fasteners
Q_{EAS}	equi-angle skew
R_{DO}	radius of the diffuser outlet
Re	Reynolds number
Re_x	local Reynolds number
R_n/Ω	available strength in weld
T	temperature
U_∞	free stream velocity
\mathbf{V}	velocity
\mathbf{V}_{CI}	contraction inlet velocity
\mathbf{V}_{CO}	contraction outlet velocity
\mathbf{V}_{av}	average velocity
\mathbf{V}_{cl}	center line velocity
\mathbf{V}_{max}	maximum velocity at the test section inlet
\dot{V}	volumetric flow rate
\dot{V}_{max}	maximum volumetric flow rate
X_C	normalized distance downstream

Lower-case Roman

a	side (also width or length)
a_C, b_C, \dots	contraction polynomial coefficients
a_{TS}	test section side/height/width
c	O-ring groove depth
c_{D1}, c_{D2}	coefficients for the diffuser geometry
c_d	desired groove depth
c_f	chord length
d_{eff}	effective diameter
d_f	fastener diameter
fps	frames per second
g	O-ring groove width
h_f	foil thickness
h_p	plate thickness
l_c	approximate window circumference
l_f	fastener contact length
l_w	length of weld
l_{wo}	length of window opening
\dot{m}	mass flow rate
n_f	(fastener) number of threads per inch
n_{fr}	number of frames
n_{tot}	total number of cells
p	pressure
p_{CI}	contraction inlet pressure
p_{CO}	contraction outlet pressure
p_{atm}	atmospheric pressure
p_g	pressure acting on O-ring groove
p_v	vapour pressure
q	load per unit area
r	radius
$squeeze$	squeeze of O-ring
$squeeze_d$	desired O-ring squeeze
t	window thickness
w	O-ring width
w_g	distance between O-ring groove and nearest edge
w_{max}	maximum deflection at the center of the window
x_C	downstream distance from the inlet of the contraction
x_D	downstream distance from the inlet of the diffuser
x_{TS}	downstream distance from the inlet of the test section
y_C	distance from the center-line at a given location, x_C downstream of the contraction inlet
y_{CI}	distance from center-line at the inlet of the contraction
y_{CO}	distance from center-line at the outlet of the contraction

Upper-case Greek

Δl	difference in elongation
------------	--------------------------

Lower-case Greek

α	angle of attack
α_g	linear coefficient of thermal expansion for PPG glass
α_s	linear coefficient of thermal expansion for 316 stainless steel
δ	boundary layer thickness
δ_1	displacement thickness
δ_{99}	boundary layer thickness
ϵ	convergence criteria
ν	kinematic viscosity

ρ	density
σ	cavitation number
σ_f	shear stress on fasteners
σ_{fa}	axial stress on fasteners
σ_g	stress on the O-ring groove
σ_{max}	maximum stress
σ_s	windows shear stress
σ_w	stress on weld
$\phi^{1/2eff}$	effective diffuser half-angle
ω	motor speed

Abbreviations

CAD	Computer Aided Design
CFD	Computational Fluid Dynamics
DTMB	David Taylor Model Basin
LDV	Laser Doppler Velocimetry
PIV	Particle Image Velocimetry
PTV	Particle Tracking Velocimetry
SAFL	Saint Anthony Falls Laboratory
UNH	University of New Hampshire

LIST OF FIGURES

1.1	Water tunnel at SAFL, before being disassembled, and tunnel components after their arrival at UNH.	2
1.2	Test section shape alternatives	2
1.3	Sketch of the water tunnel	3
1.4	Honeycomb installation options	3
2.1	Honeycomb cells	5
2.2	Schematics of contraction	6
2.3	Contraction profile	7
2.4	Transition shape	12
3.1	Sample contraction inner surface geometry	13
3.2	Cell quality	14
3.3	Velocity profiles at contraction outlet for different L/D ratios (inviscid flow)	15
3.4	Velocity profile at contraction outlet for L/D=1.0 at 50% of maximum flow rate(inviscid flow)	15
3.5	Velocity profiles at contraction outlet for different L/D ratios (viscous flow)	16
3.6	Velocity profiles at the outlet of a contraction with L/D=1.5 for different flow rates	16
3.7	Comparison between different simulations for contraction with L/D=1.5 and maximum flow rate	17
3.8	Velocity profiles at contraction outlet and at two locations downstream of it	18
3.9	Velocity profiles at test section inlet and outlet (empty test section)	18
3.10	Velocity profiles at test section inlet and outlet (with foils)	19
3.11	Velocity contour plot for test section with a foil with 75 mm chord	20
3.12	Velocity contour plot for the outlet of a short square test section	20
3.13	Diffuser simulations	21
4.1	Test section components	23
4.2	Window configurations	24
4.3	Solid Works simulation for deflection of top/bottom window	27
4.4	Sketch of weld between side plates and top/bottom plates	29
4.5	Contraction and diffuser	32
4.6	Inner surfaces of the contraction and the diffuser	32
4.7	Contraction and diffuser interfaces with test section	33
4.8	Indents on the sides of the contraction and diffuser flanges	33
4.9	Test section modifications	33
4.10	Test section before being welded together	34
4.11	Test section imperfections	34
4.12	Water tunnel upgrades	35
4.13	Installation of water tunnel components	35
4.14	Additional water tunnel upgrades	36
4.15	Force balance and hydrofoil sections	36
4.16	Assembled tunnel – Solid Works rendering	37
4.17	Assembled tunnel – picture of the tunnel	37
5.1	PTV measurements location	39
5.2	Snapshots of flow in the test section	39
5.3	Sample frames from PTV measurements	40
5.4	Schematics of light paths for the PTV experiment (top view)	40
5.5	PTV Calibration	41
5.6	Approximate velocity profile from PTV measurements	41
5.7	LDV measurements locations	42
5.8	LDV Calibration	42
5.9	LDV profiles and comparison with numerical simulation results	43

5.10	PIV measurements locations	43
5.11	PIV Calibration	43
5.12	PIV velocity contour at the middle of the test section	44
5.13	Pressure measurements locations	44
5.14	High-speed water tunnel calibration	45
A.1	Water tunnel sketch	52
B.1	Water tunnel room electrical wiring	53
C.1	Test section assembly drawing	54
C.2	Side plate drawing	55
C.3	Top/bottom plate drawing	56
C.4	Flange drawing	57
C.5	Glass window drawing	58
C.6	Retainer drawing	59
C.7	Acrylic top/bottom window drawing (no pressure holes)	60
C.8	Acrylic side window drawing	61
C.9	Acrylic top/bottom window drawing (pressure holes modification)	62

LIST OF TABLES

2.1	Comparison of test section shapes	9
2.2	Comparison of test section sizes	10
3.1	Total number of cells	14
3.2	Boundary layer thickness. Comparison between theoretical and CFD results.	19
4.1	Forces acting on test section windows	25
4.2	Windows shear stresses	25
4.3	Bending strength and center-point displacement for glass and acrylic windows	26
4.4	Windows bending and shear (Solid Works simulations)	26
4.5	Stress on fasteners	28
4.6	Grooves dimensions (nominal sizes)	30
4.7	Grooves dimensions (desired sizes)	30

CONTENTS

Abstract	i
Preface	v
Acknowledgements	v
Nomenclature	vii
List of Figures	x
List of Tables	xii
Contents	xiii
1 Introduction and Project Overview	1
1.1 Historical Background	1
1.2 Tunnel Condition and Proposed Modifications	1
1.3 Flow Circuit	2
1.4 Upper Leg of Circuit	3
2 Theoretical Studies	5
2.1 Contraction	5
2.1.1 Available Length	5
2.1.2 Contraction Shape	5
2.1.3 L/D ratio	7
2.2 Test Section	7
2.2.1 Velocity and Cavitation Number	8
2.2.2 Boundary Layer Thickness and Center-Line Velocity	8
2.2.3 Blockage Ratio	8
2.2.4 Test Section Shape	9
2.2.5 Test Section Size	10
2.3 Diffuser	11
3 Numerical Results	13
3.1 Contraction	13
3.1.1 Geometry	13
3.1.2 Inviscid Flow Simulations	14
3.1.3 Viscous Flow Simulations	16
3.1.4 Comparison with Cobalt Software	17
3.2 Test Section	17
3.2.1 Boundary Layer Growth	17
3.2.2 Additional Studies	19
3.3 Diffuser	20
4 Design, Fabrication, and Installation	23
4.1 Test Section Requirements	24
4.2 Material Thickness	24
4.3 Forces Acting on the Windows	25
4.4 Windows Shear	25
4.5 Windows Bending Moments and Displacements	25
4.6 Fasteners	27
4.7 Welds	28
4.8 O-Ring Grooves	29
4.9 Thermal Effects	31

4.10	Contraction and Diffuser Fabrication	31
4.11	Test Section Fabrication	32
4.12	Installation	34
4.13	Suggestions for Design and Installation	38
5	Experimental Results	39
5.1	PTV measurements	39
5.2	Laser Doppler Velocimetry	42
5.3	Particle Image Velocimetry	43
5.4	Pressure Measurements and Calibration Equation	44
6	Conclusion	47
	Bibliography	49
A	Water Tunnel Sketch	51
B	Water Tunnel Room Electric Wiring	51
C	Drawings	51

1 Introduction and Project Overview

1.1 Historical Background

The high speed water tunnel was originally designed as a 1:10 scale physical model for a 60-inch¹ tunnel that was going to be built at the David Taylor Model Basin (DTMB) of the U.S. Department of the Navy [16]. Work on the 6-inch tunnel started in 1946 and it was built and tested by 1948 at Saint Anthony Falls Laboratory (SAFL) at the University of Minnesota. Information about the original design, test procedures and component studies of the apparatus can be found in [12].

The full scale 60-inch water tunnel was never built at DTMB, but the original and new model studies were used in the design of a 36-inch Variable Pressure Cavitation Tunnel that was built at DTMB/Carderock in 1961. Meanwhile, the 6-inch tunnel was used for many experimental projects at SAFL, mostly in the field of cavitation. Major research performed with the use of the 6-inch tunnel include cavitation studies using controlled air nuclei and development of “Schiebe Bodies” [15].

In order to accommodate the use of a LDV system, and to more closely match the test section of the 7¹/₂-inch cavitation tunnel at SAFL, the tunnel was retrofitted with a new test section in the 1980’s. The original 6-inch circular test section was replaced with a 7-inch octagonal² test section with optical glass windows. This required a modification of the contraction; also, a short section near the end of the test section component had to be used for a 7-inch octagonal to 8-inch round transition upstream of the diffuser.

By the mid 1990’s the tunnel was not used anymore at SAFL and in 2008, it was disassembled and moved to the University of New Hampshire (UNH) by Prof. Martin Wosnik.

1.2 Tunnel Condition and Proposed Modifications

After moving the tunnel parts to UNH, the condition of the components was assessed (Fig. 1.1). The contraction and test section were significantly damaged and were considered to be unusable. The rest of the steel components were sand-blasted and powder-coated on the outside. The steel parts of the flow circuit had originally been hot-dip galvanized. The water-facing side had only mild corrosion and was considered usable after the parts were cleaned.

The damaged components (contraction, test section and transition/diffuser) had to be replaced, so a few modifications were proposed. It was decided that the test section should have a slightly smaller cross section in order to allow for a higher maximum test section velocity and hence a wider range of cavitation numbers. Three options for the shape of the test section were considered (Fig.1.2). The existing test section was octagonal (square with fillets) so that corner cross-flows and secondary flows in the contraction could be reduced [2]. The second option was to use a square test section with longitudinally diminishing fillets, to compensate for the effect of the boundary layer growth, and decrease the variation of center-line velocity. The uniform square option was also considered for purposes of providing full access for optical measurements, including measurements close to the wall.

New contraction and transition components were required for the new test section. In the previous configuration, the contraction was installed within a straight pipe and it had to be attached with bolts to the test section before being inserted in the pipe. It was decided to shorten the straight conduit, so that it would connect to the larger flange of the contraction and eliminate the complexity of installation. Also, it was decided that the (square-to-round) transition component would be

¹The size denotes the diameter for round test sections and the height (or width) for square test sections.

²7-inch square with 1-inch fillets



Figure 1.1: Water tunnel at SAFL, before being disassembled, and tunnel components after their arrival at UNH.

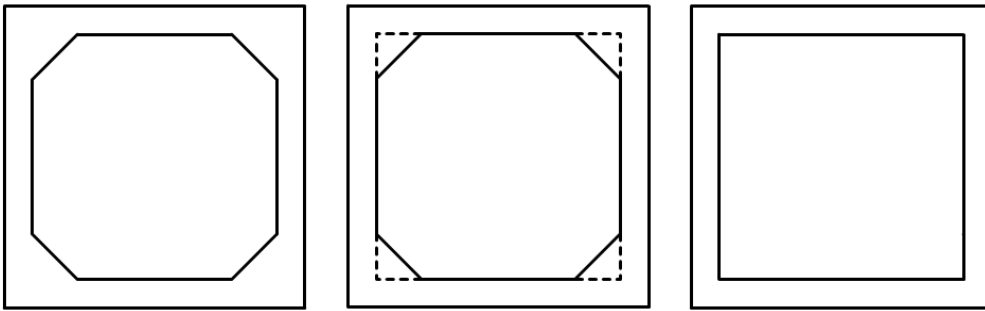


Figure 1.2: Test section shape alternatives. From left to right: square with fillets, square with diminishing fillets, and square. Flow is into the plane of the sheet.

separate from the test section, and it would serve as a diffuser, having a constant increase in cross sectional area in the stream-wise direction.

Other proposed modifications and upgrades included new tunnel supports, a new motor and drive, a system for independent pressure/vacuum control, and automated control of the test section velocity and pressure.

1.3 Flow Circuit

The final circuit of the renovated water tunnel consists of 26 major components (Fig.1.3). Downstream of the new test section (part 0), a new transition/diffuser component is installed in order to increase the cross-sectional area of the flow while changing its shape from square to round. A large 3.5° -half-angle diffuser (part 2) connects to corner 1 (parts 3 – 5)³ The corner is followed by a small 6° -half-angle diffuser (6) and corner 2 (parts 7 – 9). The drive shaft for the impeller penetrates through part 7 and extends to part 10, where the impeller is located. Parts 10 and 11 have viewing ports to observe the flow before, at and after the impeller. Part 12 is a 4° -half-angle diffuser and is followed by two straight sections (13 and 14) and corner 3 (parts 15 to 17). There is one 1-inch opening in part 14 and a smaller opening in part 15 which are used for draining. A short straight pipe - (part 18) connects to corner 4 (parts 19 – 21), which is followed by a short section (22), a

³All corners consist of two slanted pipes connected by a component with turning vanes.

honeycomb (23), the modified straight pipe (24) and the new contraction (25).

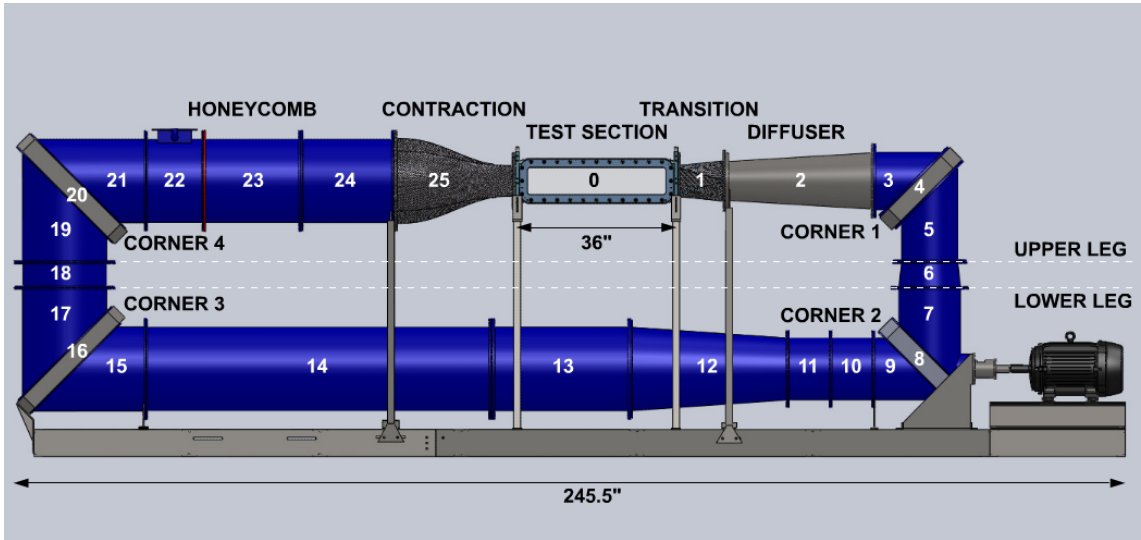


Figure 1.3: Sketch of the water tunnel. All major components are numbered starting from “part 0” – the test section – and continuing in the direction of the flow.

1.4 Upper Leg of Circuit

The overall available length for the upper leg of the water tunnel from corner 4 (downstream edge of part 21) to corner 1 (upstream edge of part 3) was measured to be 161 inches. After corner 4, a short $12\frac{5}{8}$ -inch component (part 22) was installed to allow the flow to recover after the turning vanes, before it enters the honeycomb component. This part is also used to connect the tunnel to a riser tank and a pressure/vacuum system. A honeycomb component (23) was installed downstream of this part. At one of its sides, the honeycomb extends beyond the flange of the pipe section that contains it, so it could be installed in two different ways (Fig.1.4). However, installing it with this side towards corner 4 would have shortened the space between the honeycomb and the trailing edge of the closest guiding vane from $10\frac{3}{8}$ inches to $7\frac{3}{4}$ inches. In order to leave enough space for flow recovery, it was decided that the extension would be facing downstream instead.

A straight duct was shortened (24) and installed between the honeycomb and the contraction (25). The duct was machined last, since a more accurate measurement of its desired length could be obtained after installing all other components. After the contraction, the test section and the transition component, a round diffuser was installed, and it connects to corner 1. Thus the total available length for the duct, contraction test section and transition was $94\frac{3}{4}$ inches.

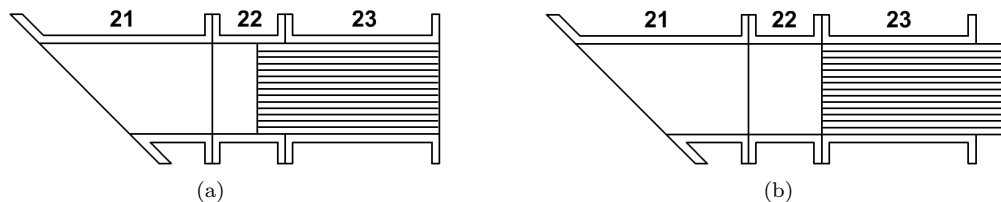


Figure 1.4: Sketch of honeycomb installation options (section view). Option (b) was selected

2 Theoretical Studies

2.1 Contraction

The design of the contraction had the following constraints:

- inlet cross section was defined by the upstream flow circuit to be circular with a diameter of 18 inches
- contraction outlet had to match the inlet of the test section
- maximum length was limited by the rest of the flow circuit

The parameters that could be varied were:

- contraction shape / equation of the curve
- Length/Diameter ratio (L/D ratio)

2.1.1 Available Length

As discussed in section 1.4, a straight duct had to be installed between the honeycomb and the contraction. Based on [8] a distance of 30-40 cell sizes between the honeycomb and the contraction is sufficient for turbulence decay. The average cell size M of the honeycomb (c.f. Fig.2.1) was estimated to be:

$$M = \sqrt{M_h M_w} = 0.514'', \quad (2.1)$$

where

$M_h = 0.461''$ is the average height of a cell, and

$M_w = 0.573''$ is the average width of a cell.

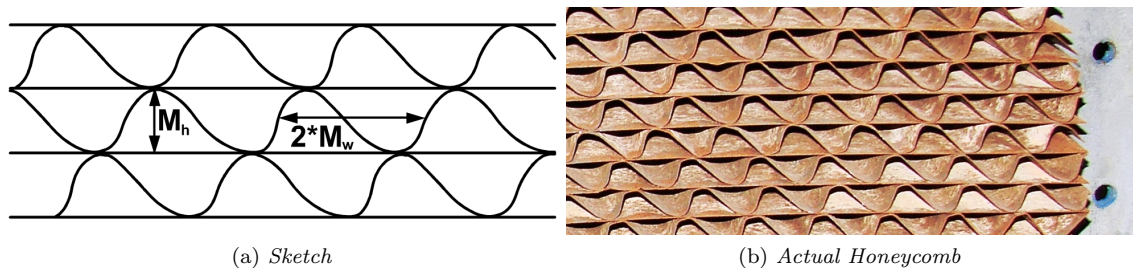


Figure 2.1: *Honeycomb cells*

Thus, approximately 20 inches ($L/M \approx 40$) had to be allocated for the straight duct. The original test section length of 36 inches was considered reasonable in order to observe the flow, downstream of a typically-sized object placed in it. The transition component was estimated to be 10 inches, assuming it acted as a typical diffuser. The existing diffuser had a length of $32^5/8$ inches. This meant that there were approximately 25 inches available for a contraction.

2.1.2 Contraction Shape

A well designed contraction should speed up the flow, decrease turbulence intensity and create a uniform flow, while avoiding separation. According to [2] “The contraction wall shape satisfying most of the requirements [...] is clearly the one given by the 5th order polynomial.” Although this analysis was done for small low-speed wind tunnels, it was decided that a fifth-order polynomial curve will be used for the water tunnel as well. Other examples of high-speed water tunnels that

use fifth-order-polynomial contractions are the LCC [19], HYKAT [1] and LOCAT [20].

The equation of the curve of the contraction at any azimuthal location should be of the form:

$$y_C = y_{CI} - (y_{CI} - y_{CO}) [a_C X_C^5 + b_C X_C^4 + c_C X_C^3 + d_C X_C^2 + e_C X_C + f_C], \quad (2.2)$$

where $X_C = x_C/L_C$ is the normalized distance downstream, x_C is the distance downstream of the contraction inlet, y_C is the radial distance from the center-line at a location x_C , y_{CI} is the radial distance from center-line at the inlet of the contraction, y_{CO} is the radial distance from center-line at the outlet of the contraction, a_C, b_C, \dots are the coefficients of the polynomial describing the shape of the contraction, and L_C is the length of the contraction (c.f. Fig.2.2).

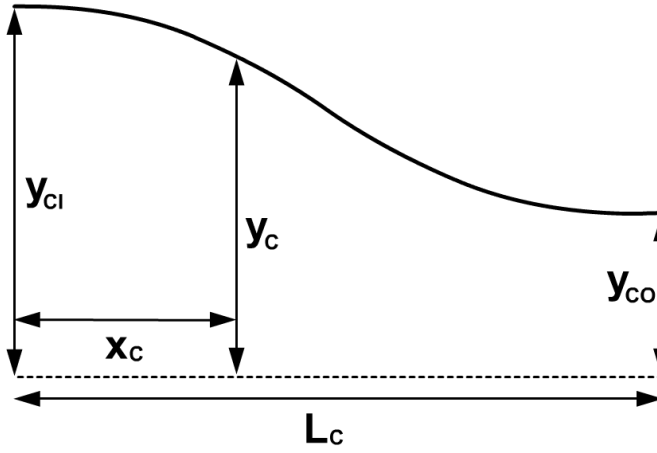


Figure 2.2: Schematics of the contraction shape. Note that the values of y_{CI} and y_{CO} vary for different azimuthal locations.

To find the coefficients $a_C, b_C, c_C, d_C, e_C, f_C$, we can use the following relations:

- $y_C(x_C = 0) = y_{CI}$ and $y_C(x_C = L_C) = y_{CO}$
- $\frac{dy_C}{dx_C} = 0$ for $x_C = 0$ and $x_C = L_C$, so that the slope of the contraction curve is 0 at the inlet and outlet of the test section
- $\frac{d^2 y_C}{dx_C^2} = 0$ for $x_C = 0$ and $x_C = L_C$, so that the curvature is 0 at the inlet and outlet
- $\frac{d^2 y_C}{dx_C^2} = 0$ for $x_C = L_C/2$, as a result of these relations - the inflection point is located half way between the inlet and the outlet of the contraction.

It can be shown that f_C, e_C, d_C are zero terms. This leads to the following equations:

- $a_C + b_C + c_C = 1$
- $5a_C + 4b_C + 3c_C = 0$
- $20a_C + 12b_C + 6c_C = 0$

Solving and setting a_C, b_C and c_C to the corresponding values of 6, -15 and 10 yields:

$$y_C = y_{CI} - (y_{CI} - y_{CO}) \left[6 \left(\frac{x_C}{L_C} \right)^5 - 15 \left(\frac{x_C}{L_C} \right)^4 + 10 \left(\frac{x_C}{L_C} \right)^3 \right] \quad (2.3)$$

The contraction shape can be seen in Fig.2.3. The slope at the inlet and outlet of the contraction is 0 and the inflection point is in the middle.

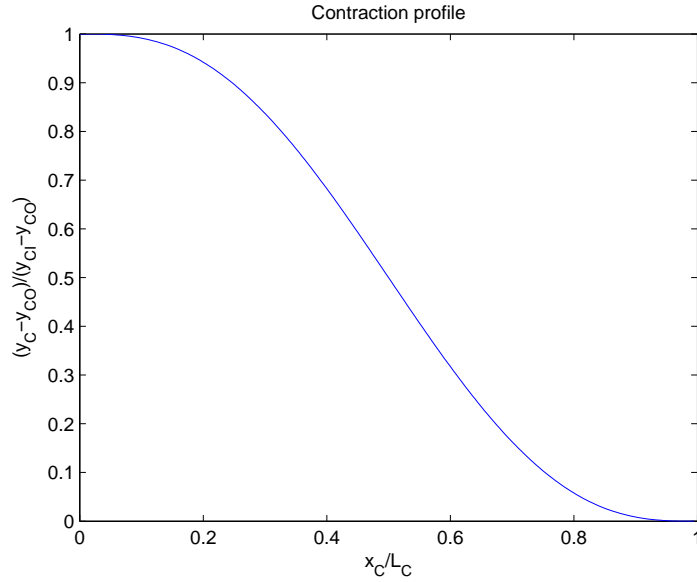


Figure 2.3: *Contraction profile, normalized by the length of the contraction on the x-axis, and on the y-axis, normalized by the difference between the radial locations of the inlet and the outlet for any given azimuthal location.*

2.1.3 L/D ratio

For rectangular contractions with a fifth-order polynomial shape, separation occurs for Length/Height ratios smaller than 0.667 and larger than 1.79 [2]. We can expect that these values would be similar for our contraction. On the other hand, based on the calculated available length (section 2.1.1), L/D ratios of more than 1.5 would require a shorter test section and/or smaller distance between the honeycomb and the contraction. To specify the length of the contraction, CFD analysis of contractions with L/D ratios from 0.5 to 1.7 was conducted in section 3.1.

2.2 Test Section

When choosing the size and shape of the test section, the following aspects were considered:

- flow speed and cavitation number ranges
- boundary layer growth and change in center-line velocity
- blockage ratios for typical experiments
- available length
- optical access and cross-flow in corners
- cost and simplicity

The parameters that could be varied were:

- test section shape
- test section size

2.2.1 Velocity and Cavitation Number

For a given volumetric flow rate \dot{V} , the average velocity at a given downstream location \mathbf{V}_{av} as a function of the cross sectional area A is:

$$\mathbf{V}_{av} = \dot{V}/A. \quad (2.4)$$

For a given pressure p , vapour pressure p_v , and density ρ of water, the cavitation number σ can be obtained from:

$$\sigma = \frac{p - p_v}{\frac{1}{2}\rho\mathbf{V}^2}, \quad (2.5)$$

for a given location at which the flow velocity is \mathbf{V} .

Equation 2.4 shows that the average velocity is inversely proportional to the area of the cross section. Since the cavitation number is inversely proportional to the square of the local velocity, a smaller test section is required to achieve smaller cavitation numbers.

2.2.2 Boundary Layer Thickness and Center-Line Velocity

According to equation 2.12 on page 34 in [13]:

$$\frac{\delta U_\infty}{\nu} = 0.14 \frac{Re_x}{\ln Re_x} G(\ln Re_x), \quad (2.6)$$

where

δ is the boundary layer thickness,

U_∞ is the free stream velocity,

ν is kinematic viscosity, and

Re_x is the local Reynolds number, which depends on the distance downstream of the test section inlet x_{TS} :

$$Re_x = \frac{U_\infty x_{TS}}{\nu}. \quad (2.7)$$

“The function $G(\ln Re_x)$ is only weakly dependent on $\ln Re_x$. It has a limiting value of 1 for $\ln Re_x \rightarrow \infty$... in the region $10^5 < Re_x < 10^6$, $G \approx 1.5$.”

Also, based on equation 2.5 on page 32 in [13] “...the displacement thickness δ_1 is about 1/3 of the boundary-layer thickness δ_{99} ”, or:

$$\delta_1 \approx \frac{1}{3}\delta_{99} \equiv \frac{1}{3}\delta. \quad (2.8)$$

Using equations 2.6 and 2.8 we can estimate the center-line velocity downstream of the test section inlet as:

$$\mathbf{V}_{cl} \approx \dot{V}/(A - 4a_{TS}\delta_1 + 4\delta_1^2), \quad (2.9)$$

where a_{TS} is the side (also height or width) of the test section.

2.2.3 Blockage Ratio

Most of the large-cross-sectional-area objects that will be placed in the test section will be hydrofoils positioned at different angles of attack.

A conservative estimate of the blockage ratio can be obtained if the foil shape is approximated to a rectangle. In this case, for a foil section occupying the entire width of the test section, the blockage ratio can be approximated to:

$$B \approx a_{TS}(c_f \sin(\alpha) + h_f \cos(\alpha))/A, \quad (2.10)$$

where

B is blockage ratio,

c_f is chord length,

h_f is foil thickness, and

α is angle of attack.

A in this case is the cross-sectional area of the test section.

2.2.4 Test Section Shape

As discussed in chapter 1.2, three different test section shapes were considered. Table 2.1 summarizes the differences among the three options.

test section shape	1" diminishing fillets	1" fillets	no fillets
\mathbf{V}_{max} [m/s]	12.76	12.76	12.06
$\Delta \mathbf{V}_{cl}$ at 100% \dot{V}_{max} [%]	6.4	13.5	12.7
$\Delta \mathbf{V}_{cl}$ at 75% \dot{V}_{max} [%]	6.6	13.8	13.0
$\Delta \mathbf{V}_{cl}$ at 50% \dot{V}_{max} [%]	7.0	14.2	13.3
$\Delta \mathbf{V}_{cl}$ at 25% \dot{V}_{max} [%]	7.7	15.0	14.0
ΔB [%]	5	5	0
ΔL_{TS} [in]	0	1.5	0
corner cross-flows	eliminated	eliminated	may be locally present
near-wall optical measurements possible	NO	NO	YES
cost & complexity	most complex	complex	least complex

Table 2.1: Comparison of test section shapes

\mathbf{V}_{max} is the maximum achievable velocity at the inlet of the test section (assuming uniform velocity profile), corresponding to the maximum possible volumetric flow rate $\dot{V}_{max} = 280$ l/s.¹

$\Delta \mathbf{V}_{cl}$ is the % change in center-line velocity between the inlet and outlet of a 36-inch-long test section, calculated using equation 2.6 with $G = 1.5$.

ΔB is the change in blockage ratio based on the change in inlet cross-sectional area²

ΔL_{TS} is the additional length that the diffuser should have to accommodate for a smaller cross-sectional area of the outlet of the test section. Consequently, the test section should be shorter by the same distance.

First, diminishing and non-diminishing fillets were compared. For diminishing fillets, the advantages are:

- boundary layer growth is compensated by the increasing cross-sectional area; hence, change in center-line velocity can be minimized
- a minor increase in the available length for the test section

the disadvantage is:

- high complexity and cost

Although diminishing fillets provide a partial solution to the problem with increasing center-line velocity, they do not eliminate the problem completely. The diminishing fillets can be designed to

¹Calculations were performed assuming that the original pump and motor configuration are used, the test section size is 6 inches, the thickness of the boundary layer at the inlet of the test section is negligible. Also, if we treat the boundary layer as laminar close to the inlet, the thickness of the boundary layer at the outlet will change by 0.16 mm.

²compared to the cross sectional area for the no-fillets case

eliminate the problem only at a certain flow rate, since the boundary layer growth is a function of the Reynolds number. Also, their effect is more notable far downstream, where the boundary layer is thickest. On the other hand, the complexity and cost associated with the design and manufacturing of a test section with diminishing fillets is significant. The additional available length for the test section was not a significant factor in the decision to rule out the diminishing-fillets option.

Next, the non-diminishing-fillets and the no-fillets options were compared. For no-fillets, the advantages are:

- simplicity and cost
- possibility of optical flow measurements close to the wall
- a minor increase in the length available for test section
- slightly smaller blockage ratio
- slightly smaller change in center-line velocity

the disadvantages are:

- slightly decreased maximum achievable velocity
- possible presence of cross-flow in the corners

The slight decrease in maximum velocity, just as the other minor differences between the two options, are based on the difference in area. The only disadvantage due to the shape then, is the possibility of occurrence of corner cross-flows. Nevertheless, even if they are present, they remain localized in the absence of separation [2]. Thus the low cost and the ability to measure close to the wall outweighed the disadvantages in this case, and the shape of the cross section of the test section was selected to be square with no fillets.

2.2.5 Test Section Size

The size of the test section affects the maximum (and minimum³) test section velocity, the cavitation number, the change in center-line velocity, the blockage ratio, and the available length for the test section. The 6-inch option was chosen as a good compromise between high achievable speed and reasonable blockage ratio (Table 2.2).

test section size [in]	7	6.5	6	5.5	5
\mathbf{V}_{max} [m/s]	8.9	10.27	12.06	14.35	17.36
σ []	0.45	0.33	0.24	0.17	0.12
$\Delta \mathbf{V}_{cl}$ at 100% \dot{V}_{max} [%]	10.9	11.7	12.7	13.8	15.2
$\Delta \mathbf{V}_{cl}$ at 25% \dot{V}_{max} [%]	12.1	13.0	14.0	15.3	16.9
$B(100 \text{ mm chord})$ [%]	8	9	10	11	12
$B(50 \text{ mm chord})$ [%]	9	10	11	12	13
ΔL_{TS} [in]	+9.2	+4.6	0	-4.6	-9.2

Table 2.2: Comparison of test section sizes

The values in the table were computed using the following information:

- vapour pressure of water was set to $v_p = 2.339$ kPa which corresponds to temperature⁴ of 20°C [3]

³The newly installed motor is capable of maintaining minimum speed equal to 10% of the maximum speed.

⁴Higher temperature will result in lower minimum cavitation number.

- minimum pressure achievable in the test section⁵ was estimated to be 20 kPa
- blockage B was calculated for a NACA0015 foil with 100 mm chord at 0° angle of attack and 50 mm chord at 10° angle of attack. Using equation 2.10 for angles of attack of 2, 5, 10 and 20 degrees for the 100 mm foil in a 6 inch test section, the blockage ratio is 12, 16, 21 and 32%
- ΔL_{TS} was calculated assuming that a 3.5°-half-angle diffuser is used

Note that the older test section had a 7-inch octagonal cross section which is comparable to the 7-inch square option in the table.

2.3 Diffuser

The transition/diffuser component design was limited by:

- inlet of the transition had to match the 6-inch square cross section of the outlet of the test section
- outlet of the transition had to match the 8¹/₁₆-inch diameter of the downstream part (2), a long round diffuser
- length had to be minimized

The following parameters could be varied:

- shape
- length (effective half-angle)

In order to increase the available length for the test section, it was decided that the square-to-round transition would serve as a diffuser. Also, in order to ensure that it acts as a diffuser throughout its entire length, the change of cross sectional area per unit length was set to a constant c_{D1} , or:

$$\frac{dA(x_D)}{dx_D} = c_{D1}, \quad (2.11)$$

and therefore

$$A(x_D) = A_{DI} + c_{D1}x_D, \quad (2.12)$$

where:

A_{DI} is the cross sectional area at the inlet of the diffuser, and x_D is the downstream distance from the inlet of the diffuser.

Now c_{D1} can be determined from:

$$c_{D1} = (A_{DO} - A_{DI})/L_D, \quad (2.13)$$

where A_{DO} is the cross sectional area of the diffuser outlet and L_D is the length of the diffuser. At any location x_D , the cross sectional area of the diffuser $A(x_D)$ consists of an inner square “core” with length $a(x_D)$ - denoted by a dashed line in Fig. 2.4 - and a rounded corner with radius $r(x_D)$. Thus the area at a location x_D is also:

$$A(x_D) = a(x_D)^2 + 4r(x_D)a(x_D) + \pi r(x_D)^2. \quad (2.14)$$

We have one equation and two unknowns, so we must constrain one of the variables. In order to simplify the process of modeling the shape in CAD software, we let the radius have a linear dependence on x_D :

$$r = c_{D2}x_D, \quad (2.15)$$

⁵The vacuum system purchased for the water tunnel is capable of achieving pressure of 0.2 kPa. However, the pressure at the pump should not decrease below the vapour pressure of water, in order to avoid damage to the pump. Furthermore the water level height and any water tunnel sealing imperfections will limit the minimum pressure value.

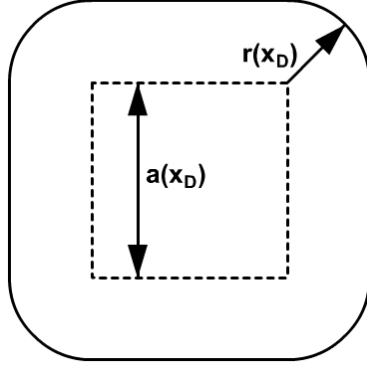


Figure 2.4: *Transition cross-section shape at a location, x_D downstream of the transition inlet. At the inlet of the transition $r(x_D) = 0$ and $a(x_D)$ is equal to the width/height of the test section. At the transition outlet, $r(x_D)$ is equal to the radius of the round diffuser and $a(x_D) = 0$*

and

$$c_{D2}L_D = R_{DO}. \quad (2.16)$$

Substituting r in 2.14 and equating 2.12 and 2.14 leads to:

$$A_{DI} + c_{D1}x_D = a(x_D)^2 + 4c_{D2}x_D a(x_D) + \pi c_{D2}^2 x_D^2. \quad (2.17)$$

Solving the quadratic equation for $a(x_D)$ and eliminating the non-physical negative root:

$$a(x_D) = -2c_{D2}x_D + \sqrt{(4 - \pi)c_{D2}^2 x_D^2 + A_{DI} + c_{D1}x_D}. \quad (2.18)$$

This solution satisfies the following conditions:

at the inlet of the diffuser, where $x_D = 0$:

- $a(0)^2 = A_{DI}$ and $r(0) = 0$

at the outlet of the diffuser, where $x_D = L_D$:

- $a(L_D) = 0$ and $\pi r(L_D)^2 = A_{DO}$

The second parameter - length, which is determined by the effective half-angle, was selected after CFD analysis.

3 Numerical Results

For the numerical simulations, CAD models of the contraction, test section, and diffuser were created using Pro/ENGINEER Wildfire 4.0 [10]. These models were imported in Gambit 2.4.6 [6] where they were meshed and their boundary conditions were specified. Finally simulations were run using Fluent 6.3.26 [5].

3.1 Contraction

The main goal of the contraction simulations was to investigate how the different length over diameter (L/D) ratios affect the flow field. This was done in order to determine a reasonable balance between length of the contraction and flow uniformity at its outlet.

3.1.1 Geometry

The exact shape of the contraction was created by defining twelve curves using the fifth-order polynomial (equation 2.3) for different azimuthal locations (in a cylindrical coordinate system with coordinate axis coinciding with the center-line of the contraction). Surfaces were defined by the curves and by the edges of the cross-sectional areas of the inlet and outlet.

At the time of the simulations, it was assumed that the test section would resemble the existing configuration and have fillets, hence most of the simulations were performed for octagonal outlet cross-section of the contraction (6-inch square with 1-inch and 1¹/₄-inch fillets - Fig.3.1). The L/D ratios studied with these geometries were 0.5, 0.8, 1.0, 1.1, 1.3, 1.5 and 1.7¹. Other geometries, including contractions for smaller and larger test sections were studied as well, but they will not be discussed further in this work.

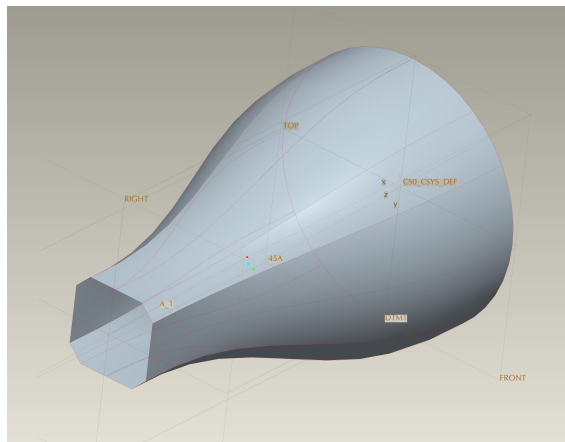


Figure 3.1: *Sample contraction inner surface geometry exported from Pro/Engineer. The contraction surface shown on the figure has a L/D ratio of 1.5 and a 6-inch square with 1-inch fillets outlet.*

It was not expected to observe recirculation within the contraction (for most cases), so the geometric boundaries for the simulation were set $1/4D$ upstream of the inlet (for the incoming flow), and $1/2D$ downstream of the outlet of the contraction (for the outgoing flow), in order to properly capture the flow features. As discussed in [18] “Commonly outflow boundaries are positioned at locations where the flow is approximately unidirectional...”. The boundary conditions in Fluent were set to

¹L/D ratio of 1.7 was studied only for the 1¹/₄-inch-fillets geometry.

velocity inlet, pressure outlet and walls.

Hexahedral cells were used to mesh the studied domain. For the 6-inch section with 1¹/₄-inch fillets, between 80 000 and 300 000 cells were used (larger number corresponding to larger L/D ratio). For the 6-inch section with 1-inch fillets, the total number of cells n_{tot} was between 150 000 and 440 000 and the exact values are shown in table 3.1. The percentage of cells with Equi-angle skew Q_{EAS} of less than 0.2 is more than 83 for all cases except for L/D = 0.5 where 80% of the cells meet this criteria². In Fig.3.2 the meshed geometry for the 0.5 L/D Contraction is shown.

L/D	0.5	0.8	0.9	1.0	1.1	1.2	1.3	1.4	1.5
n_{tot}	153 105	234 871	263 900	292 929	320 287	349 800	376 442	405 603	436 568

Table 3.1: Total number of cells

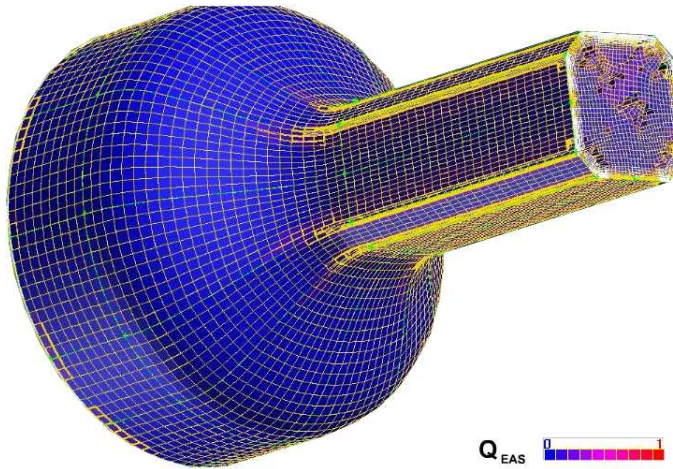


Figure 3.2: *Quality of cells for a contraction geometry with L/D ratio of 0.5. The missing cells are with lower quality, corresponding to high value of Q_{EAS} . The yellow lines separate different cells.*

3.1.2 Inviscid Flow Simulations

In [2] it was shown that inviscid flow simulations combined with boundary layer calculations agree well with experimental data. To obtain a quick approximate estimate of the flow at the outlet of the contraction, inviscid simulations were performed.

For each geometry, the velocity at the inlet boundary condition was set to 1.7, 1.275, and 0.85 m/s corresponding to 100%, 75%, and 50% of \dot{V}_{max} where \dot{V}_{max} is the maximum volumetric flow rate documented in [12] of 280 l/s. The pressure at the outlet boundary condition was set to 0 Pa gauge pressure.

Second order discretization scheme was used for the pressure, and second order upwind discretization scheme was used for the remaining terms of the equations. SIMPLE algorithm was used for pressure-velocity coupling. The under-relaxation factors were kept above 0.7 for most of the equations, except for the equation for pressure. Lower factors were used in the occurrences when the solution would not converge. Convergence criterion (non-dimensional normalized residuals) were set to 0.001 for all equations.

The velocity profiles at the outlet of the contractions were compared for different geometries. All of

² Q_{EAS} is an important measure of quality of cells. Cells with $0 < Q_{EAS} < 0.25$ are considered to be of excellent quality while cells with $0.9 < Q_{EAS} < 1$ are considered to be of poor quality.

them exhibit an “overshoot” close to the wall and a lower center-line velocity (Fig.3.3). At higher L/D ratios, the flow at the outlet was more uniform. For L/D ratio of 1.5 the velocity variation between the maximum velocity and the velocity at the center-line is slightly larger than 1% of the mean velocity, and for L/D of 1.7 it is below 1% of the mean velocity. However, L/D ratio of 1.7 was not acceptable, as discussed in section 2.1.3. Also, it was observed that for smaller velocities, the flow is much more uniform (Fig. 3.4).

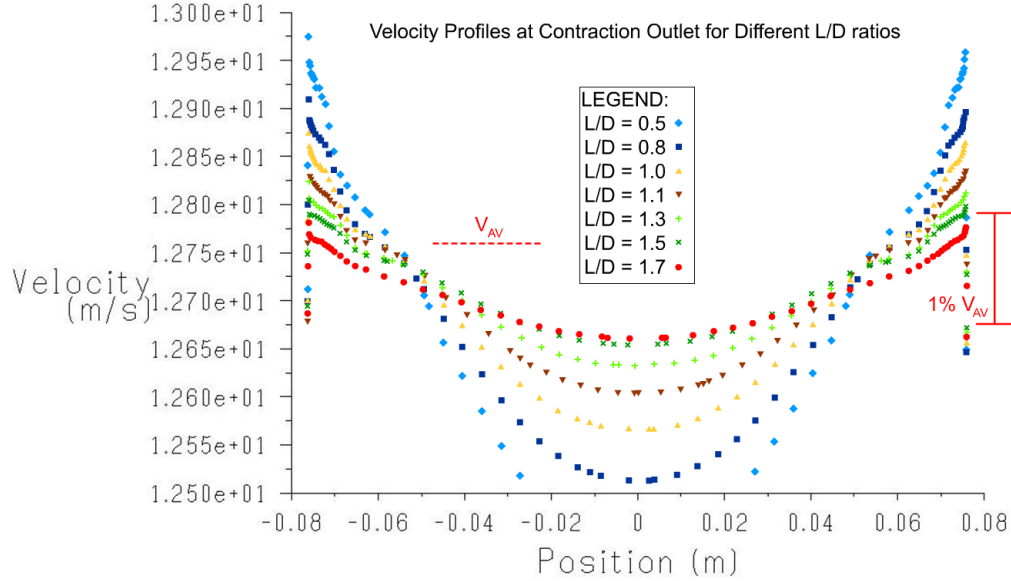


Figure 3.3: Velocity profiles at the outlet of contractions with different L/D ratios - inviscid flow simulations for the case of maximum achievable flow rate with the old motor. Note the range of the scale on the y-axis. On the x-axis, 0 m corresponds to the center-line

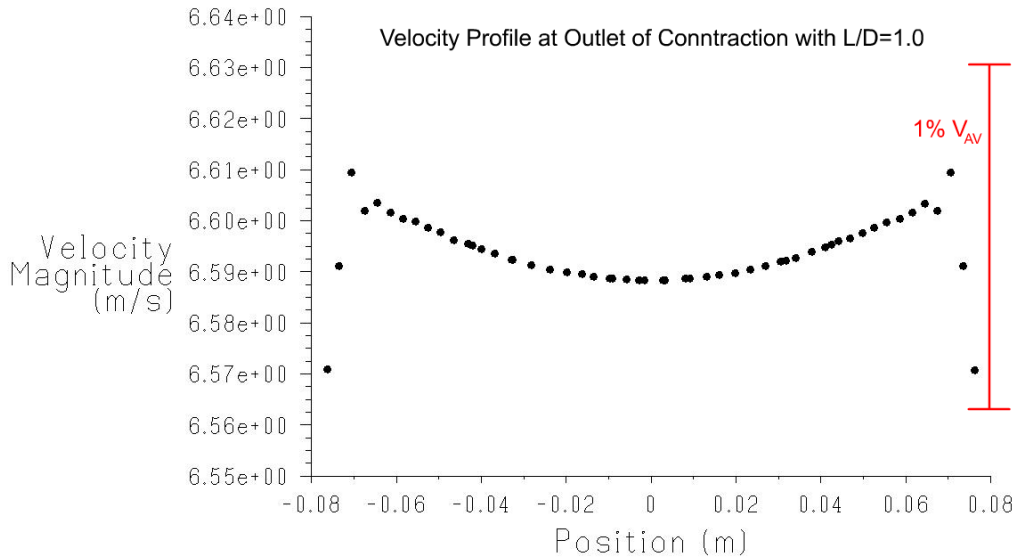


Figure 3.4: Velocity profiles at the outlet of a contraction with L/D ratio of 1.0. Inviscid flow simulations for the case of 50% of the maximum achievable flow rate $\dot{V}_{max}=280$ l/s.

3.1.3 Viscous Flow Simulations

The results from the inviscid flow simulations showed that the main reason for non-uniformity of the flow, at the outlet of the contraction, is the overshoot of velocity close to the wall. In a viscous flow, it was expected that the presence of a boundary layer would dampen the overshoot, hence contractions with lower L/D ratios would satisfy the requirement for 1% variation of the stream-wise velocity outside of the boundary layer. On the other hand, the advantage of having additional length for the test section would have been offset by any non-uniformities if a very short contraction was selected. For the viscous flow simulations, only L/D ratios of 1.3, 1.4 and 1.5 were of interest. Similarly to the inviscid flow simulations, velocity at the inlet was set to 100%, 75%, and 50% of V_{max} . The turbulence model chosen for this set of simulations was $k - \omega - SST$. As mentioned in [4], this model is a combination of the $k - \epsilon$ and $k - \omega$ models. Hence, this was a suitable 2-equation model for the viscous simulations. All other parameters were the same in the inviscid and viscous simulations.

For all three geometries, the velocities at the outlet of the contraction, outside of the boundary layer, do not vary by more than 1% (Fig.3.5). Also, as in the inviscid flow simulations, the flow is more uniform for lower flow rates (Fig. 3.6). However, for lower velocities, the boundary layer that grows inside the contraction is larger, as can also be seen in Fig. 3.6.

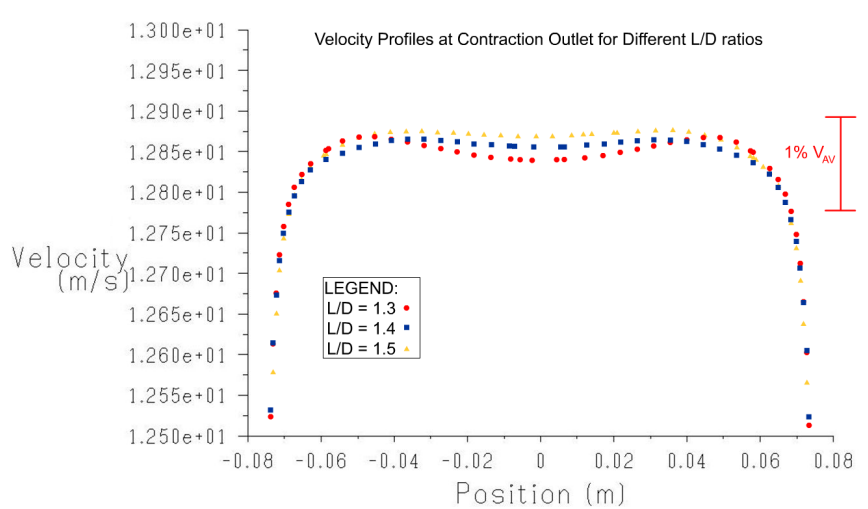


Figure 3.5: Velocity profiles at the outlet of contractions with different L/D ratios. Viscous flow simulations for the case of maximum achievable flow rate \dot{V}_{max} from [12].

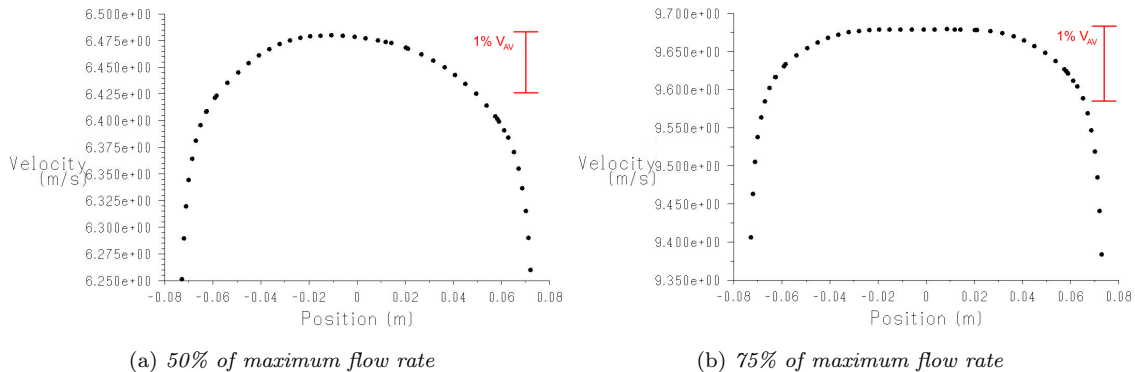


Figure 3.6: Velocity profiles at the outlet of a contraction with L/D=1.5 for different flow rates

3.1.4 Comparison with Cobalt Software

Based on the simulations results and the available space for the contraction, a L/D ratio of 1.5 was chosen. Thus the test section would be of similar length as the original one, and the flow uniformity would be excellent. Further CFD studies were conducted for the given L/D ratio and maximum flow rate. The studies included comparisons with a convergence criteria of $\epsilon = 10e - 5$, and a geometry with refined mesh in the boundary layer region (and $\epsilon = 10e - 5$). Prof. Jim Forsythe at UNH provided results from a simulation run with the same geometry. He used Cobalt Software³, which is specifically designed for air-flow simulations. Hence, he matched the Reynolds number and rescaled the results in order to give us a comparable profile (Fig.3.7). The different Fluent results follow the same trends and are extremely similar, which suggests that further refinement of the mesh or decreasing of the convergence criteria would be unlikely to yield different results. The Cobalt results seem to be different, but we have to account for the fact that the range of the velocity scale (on the vertical axis) is very small, and that the Cobalt simulation was performed for air at a matching Reynolds number which might have made compressibility effects non-negligible. Finally, a $k - \epsilon$ model was used in Fluent with all other conditions remaining the same, but no significant differences were found.

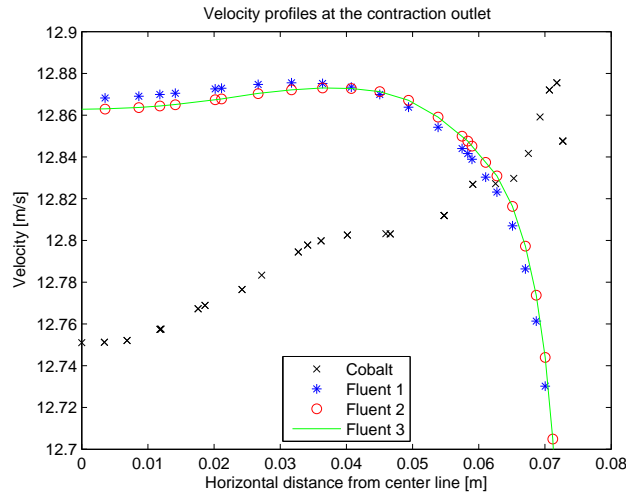


Figure 3.7: Comparison between different simulations for contraction with $L/D=1.5$ and maximum flow rate. “Fluent 1” represents the original simulation, “Fluent 2” corresponds to better convergence, and “Fluent 3” is data for better convergence and refined mesh of the boundary layer.

3.2 Test Section

The main goal of the Test Section studies was to investigate the boundary layer growth and to observe the effects of a hydrofoil installed near the inlet of the test section.

3.2.1 Boundary Layer Growth

The geometry for contraction simulations had a boundary placed $1/2D$ downstream of the contraction outlet. Thus, it provided us with not only the boundary layer thickness at the outlet of the contraction, but also with a first estimate of the boundary layer growth. On Fig.3.8, the velocity profiles for a few locations downstream of the outlet are plotted, based on the refined (Fluent 3) simulations and the Cobalt simulations of the contraction, discussed in section 3.1.4.

Four other simulations were performed for the flow in the test section at maximum flow rate. One of the simulations was done for a 35.015-inch-long empty test section (case 1; Fig.3.9), and the rest

³Prof. Forsythe was one of the four co-owners of Cobalt Solutions LLC and served as Director of Research in the company.

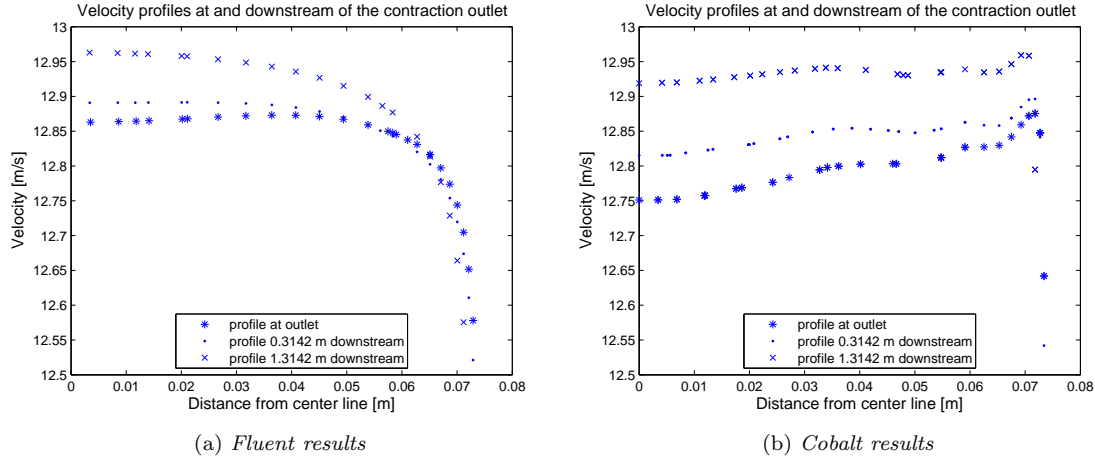


Figure 3.8: Velocity profiles at contraction outlet and two locations downstream of it.

were done for a 40-inch-long test section with a NACA 0015 foil at 10^0 angle of attack and chord lengths of respectively 50, 62.5 and 70 mm (cases 2, 3, and 4; Fig.3.10).

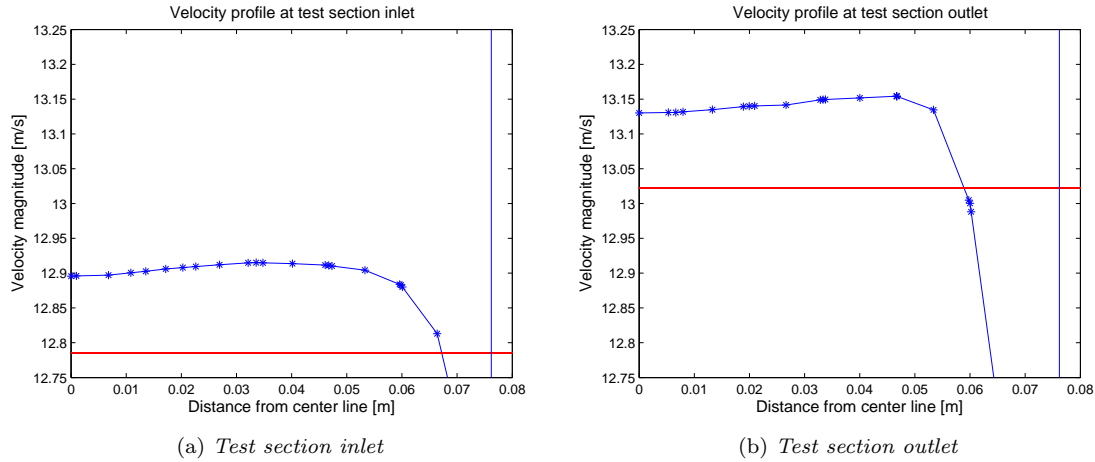


Figure 3.9: Velocity profiles at test section inlet and outlet for an empty test section. The straight vertical line represents the location of the test section wall, and the horizontal line corresponds to 99% of the average velocity for the corresponding downstream location. The intersect between this line and the velocity profile is located one boundary layer thickness away from the wall.

The number of cells was over 1 000 000 for all of the simulations⁴, and all other simulation parameters and settings were kept the same as in the contraction simulations mentioned above. In Fig.3.9, it can be seen that the boundary layer grows downstream, and as a result, the center-line velocity increases. In Fig.3.10, the boundary layer grows as well, however, the center-line velocity has decreased downstream, since the velocity profile is shown for a line parallel to the foil leading edge, positioned in the wake of the foil. For all four simulation cases, the boundary layer thickness was found and compared to a theoretically computed one. First, based on the boundary layer thickness at the inlet of the test section, the upstream location of an imaginary onset of the boundary layer was found using equations 2.6 and 2.7. Then, using the same equations, the boundary layer thickness was computed for the outlet of the test section, accounting for this additional distance. It can be seen in table 3.2 that the simulations over-predicted the boundary layer growth, by 10-17%, compared to these theoretical values.

⁴This was the total number of cells for the geometry, which included contraction, test section and two diffusers.

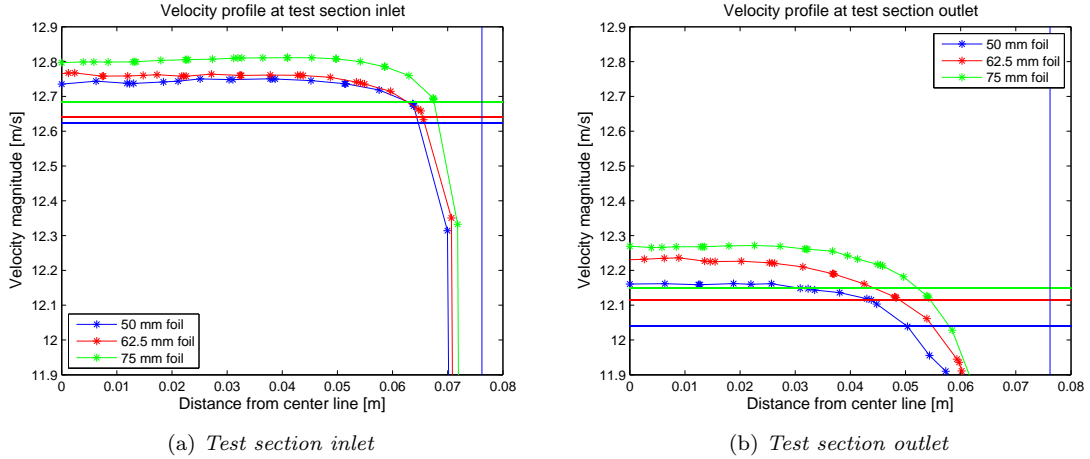


Figure 3.10: Velocity profiles at test section inlet and outlet for a test section with NACA 0015 foils at 10° angle of attack. Note that the profile at the test section outlet is for a line parallel to the foil leading/trailing edge, located in the middle between the top and bottom windows. Hence the center line velocity is decreased due to the wake of the foil.

		δ [mm] THEORETICAL	δ [mm] CFD	DIFFERENCE %
case1	no foil	19.9	24.0	17
case2	50 mm foil	23.5	26.0	10
case3	62.5 mm foil	22.8	27.2	16
case4	75 mm foil	20.8	24.0	13

Table 3.2: Boundary layer thickness. Comparison between theoretical and CFD results.

3.2.2 Additional Studies

As discussed in section 3.2.1, simulations were performed for the case of a foil installed near the inlet of the test section. A velocity contour plot of a vertical slice through the center-line of the test section can be seen in Fig. 3.11. The effect of the blockage (which is 14% for this case, can be seen, especially on the suction side of the foil. The boundary layer growth can be observed as well.

Another simulation was run for a quarter section of the test section, with no contraction upstream, a square section with no fillets, and slightly smaller length (31 inches). The goal was to observe if undesirable effects would be present in a square test section. The Reynolds Stress Model (available in Fluent [5]) was used on a geometry with close to 1 000 000 cells⁵ (Fig. 3.12). No significant corner effects were observed.

⁵The exact number is 998 250.

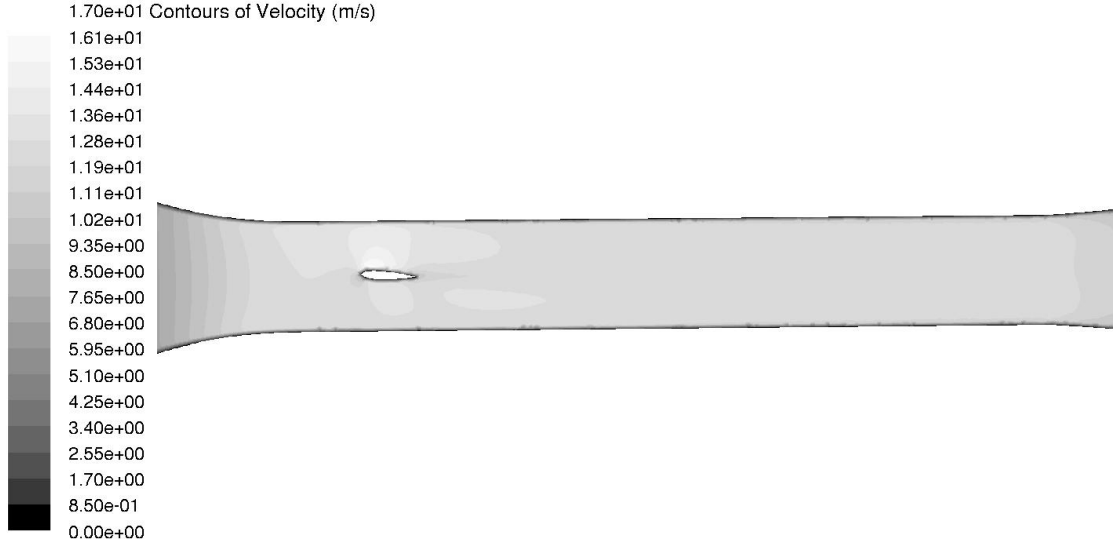


Figure 3.11: *Velocity contour plot for a test section with a foil with 75 mm chord*

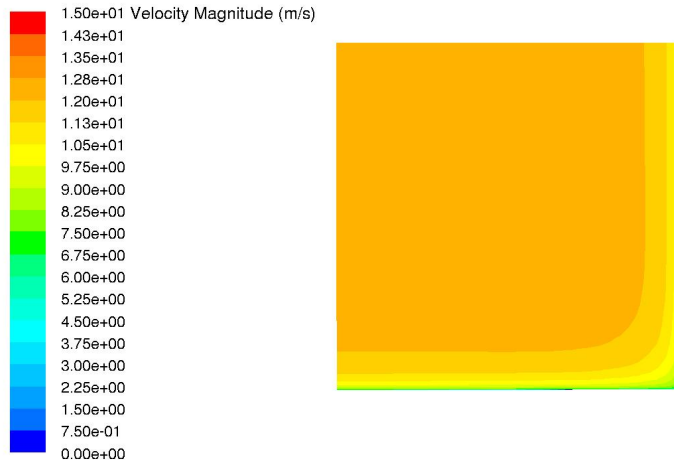


Figure 3.12: *Velocity contour plot at the outlet of a 31-inch-long, square test section. Only one quarter of the test section was observed, and symmetry boundary conditions were used.*

3.3 Diffuser

The diffuser shape was determined in section 2.3. In order to determine the length of the diffuser, an effective diffuser half-angle $\phi_{1/2eff}$ is introduced:

$$\phi_{1/2eff} = \arctan((D_2 - d_{eff})/(2L_D)), \quad (3.1)$$

where D_2 is the diameter of the inlet of the existing diffuser (part 2), and L_D is the length of the new diffuser (part 1).

$d_{eff} = \sqrt{4a_{TS}^2/\pi}$ is the effective diameter of the outlet of the test section, where a_{TS} is the test section side (also height or width).

Larger half-angles would allow the use of a shorter diffuser, resulting in more available length for the test section. However, above a certain diffuser half-angle, separation will occur. In [12], separation is

observed in the studied 5°-half-angle conical diffuser. Also in [12], experiments performed by Nikuradse are discussed. Nikuradse had shown that in a diverging rectangular conduit, non-symmetrical velocity distributions first occur at half-angle of 4°. Since the transition/diffuser component, has a more complex shape than a conical or rectangular diffuser, the use of more conservative effective half-angles was suggested.

Two simulations were performed for the transition/diffuser component. The geometry included the contraction, test section, and the new (transition) diffuser for both simulations. The existing diffuser (part 2) was included in the simulations of the final design for which only a quarter of the domain was studied, since symmetry boundary conditions were used. The total number of cells was over 1 000 000 for each of the simulations. All other variables and settings were the same as in previous simulations. Again, $k - \omega$ SST model was used, as it was expected to provide reasonable results since it does not over-predict the shear stress in adverse pressure gradient as the $k - \epsilon$ model does [4]. First, a simulation with half-angle of 3° showed no separation, so a simulation for half-angle of 3.5° was performed as well (Fig.3.13). As it did not show any separation either, it was decided that an effective half-angle of 3.5° would be used for the transition/contraction component, since at this angle, the available length for the test section was sufficient, and at a higher angle, the risk for flow separation is higher⁶.

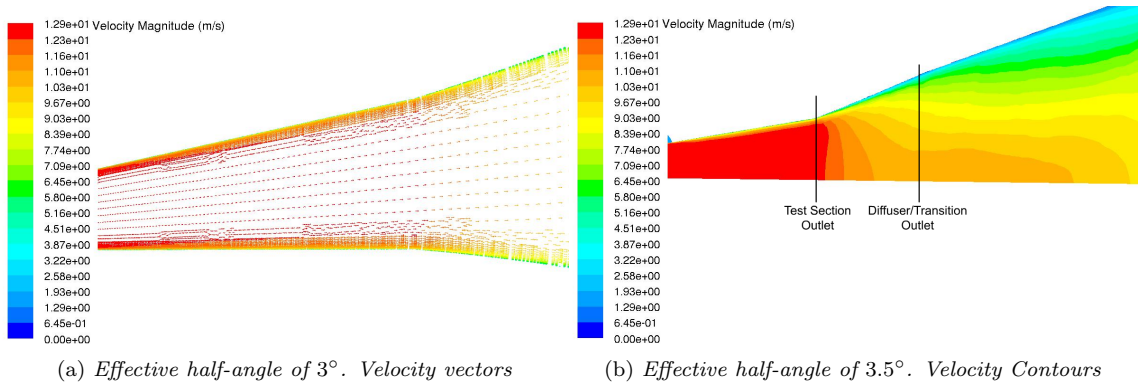


Figure 3.13: *Diffuser simulations.*

⁶The difference between required lengths for the diffusers with half-angles of 3.5° and 4° is only 1.3 inches.

4 Design, Fabrication, and Installation

The design of the contraction and diffuser was rather simple. The inner side shapes, the flange dimensions, and the strength requirements for the components were provided to a composites fabricator, who manufactured the parts. One of the major concerns for the contraction design was the axial force acting on it (F_a), which is due to the pressure difference between the inlet and the outlet, and the change of momentum of the fluid:

$$F_a = p_{CI}A_{CI} - p_{CO}A_{CO} + \dot{m}(\mathbf{V}_{CO} - \mathbf{V}_{CI}) - p_{atm}(A_{CI} - A_{CO}), \quad (4.1)$$

where p_{CI} and p_{CO} are respectively the inlet and outlet pressures, which can be related by the Bernoulli's equation,

A_{CI} and A_{CO} are the inlet and outlet areas of the contraction,

\dot{m} is the mass flow rate,

\mathbf{V}_{CI} and \mathbf{V}_{CO} are the inlet and outlet velocities, which can be related by the continuity equation, and p_{atm} is the atmospheric pressure.

At 12 m/s and 200 000 Pa test section pressure, the axial force on the contraction reaches up to 22807 N. Accounting for the hoop stress as well, the contraction and diffuser were fabricated with a minimum factor of safety of 7.

The design of the test section, was more challenging, and hence it is discussed in detail in this chapter. The frame of the final design consisted of four plates with window openings. The plates were welded together, and welded to the two flanges (Fig.4.1). The top and bottom windows were made out of acrylic. Two sets of side windows were designed - acrylic windows which mount directly to the frame, and glass windows¹ kept in place by a retainer plate (Fig.4.2). A complete set of drawings of the test section can be seen in Appendix C.

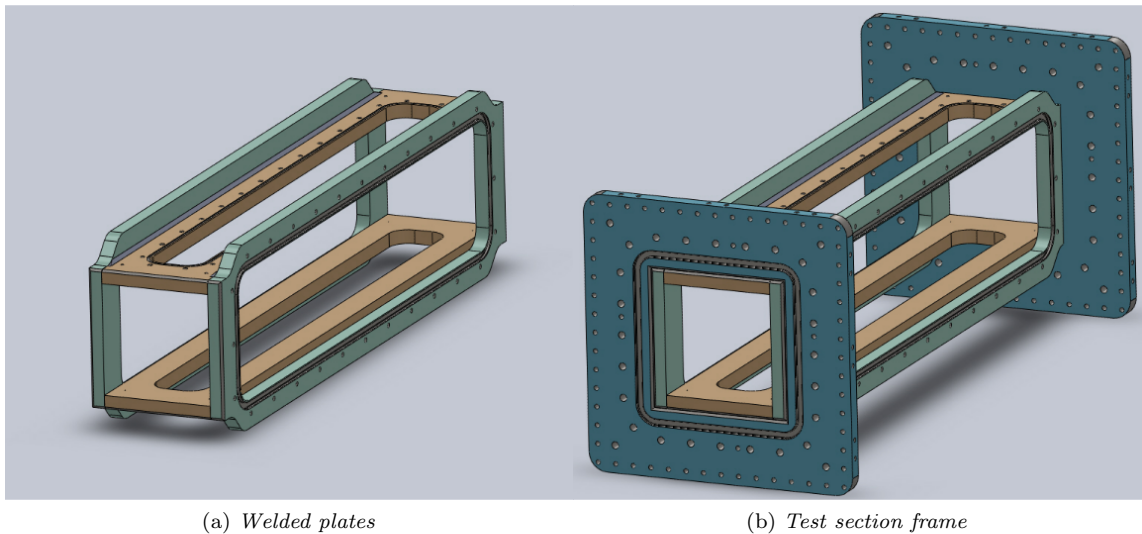


Figure 4.1: *Test section components*

¹The acrylic windows can be easily modified for various experiments, but do not have the optical quality of glass windows.

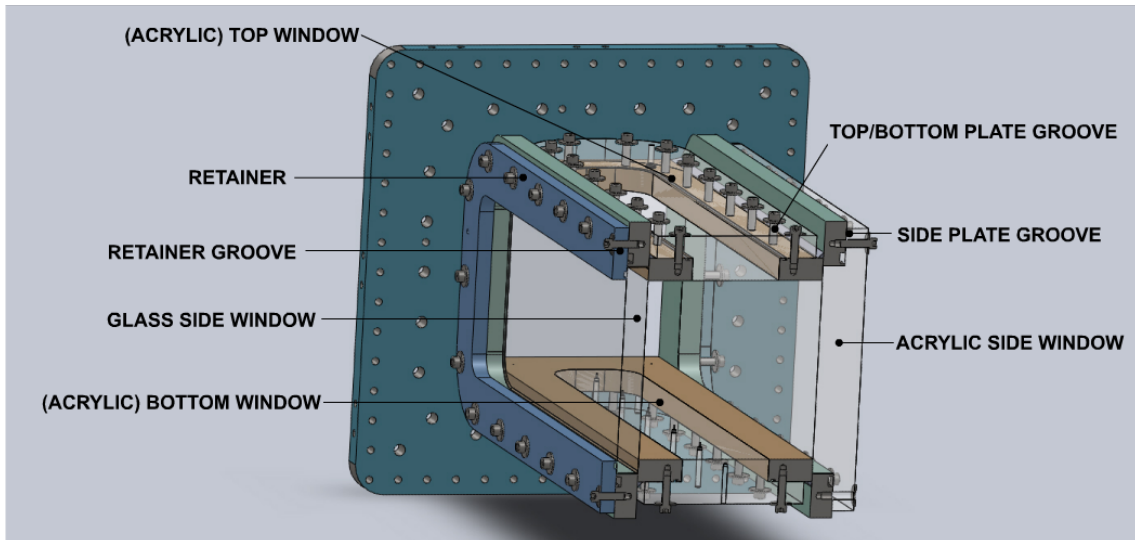


Figure 4.2: *Window configurations*

4.1 Test Section Requirements

- length – 36 inches
- cross section – 6 inches \times 6 inches
- optical access over the entire height of the test section (6 inches) from sides (i.e. visible bottom and top flow surfaces²)
- interchangeable optical quality glass/acrylic windows on the sides
- optical access from top and bottom
- simple installation of windows
- operation in the range of 20-200 kPa (absolute pressure)

4.2 Material Thickness

For the final design, the thickness of each of the materials for the test section was selected as follows:

- glass side windows³ - 0.75 inches
- side, top, and bottom acrylic windows – 1.5 inches
- stainless steel plates – 0.75 inches
- flanges – 0.75 inches
- retainer for glass windows – 0.5 inches

²In its final design, the test section can be rotated by 90°, effectively making the side windows - top and bottom windows, and vice versa.

³Note that PPG Starphire Glass was used - it has higher modulus of elasticity, similar modulus of rupture and higher thermal expansion coefficient than regular soda lime glass.

4.3 Forces Acting on the Windows

Based on the maximum desirable pressure difference between the inside and the outside of the test section, the force acting on a window was estimated to be: (equation 4.2, and table 4.1)

$$F = \Delta p A_W, \quad (4.2)$$

where F is the force acting on the window,
 Δp is pressure difference between the two sides of the window,
 A_W is window area.

	large (side) window	small (top/bottom) window
Δp [kPa]	100	100
A_W [in ²] ([m ²])	190 (.123)	115 (.074)
F [kN]	12.259	7.419

Table 4.1: Forces acting on test section windows

4.4 Windows Shear

The windows shear stress σ_s is:

$$\sigma_s = F/A_s, \quad (4.3)$$

where F is the force acting on the windows,
and A_s is the shear area, defined by:

$$A_s = l_c t, \quad (4.4)$$

where l_c is the circumference of the window shape (window was assumed to be rectangular), and t is the thickness of the window.

	glass window	acrylic side window	acrylic top window
F [kN]	12.259	12.259	7.419
l_c [in] ([m])	75 (1.9)	75 (1.9)	70 (1.8)
t [in] ([mm])	0.75 (19)	1.5 (38)	1.5 (38)
A_s [m ²]	0.036	0.073	0.068
σ_s [kPa]	338	165	110

Table 4.2: Windows shear stresses

These values for shear stress are orders of magnitude smaller than the shear strengths of the materials, which are tens of MPa for both glass and acrylic.

4.5 Windows Bending Moments and Displacements

According to [7], for a rectangular plate, clamped at all four sides, the maximum bending moment per unit length $(M_x)_{max}$ is :

$$(M_x)_{max} = C_1 q L_1^2, \quad (4.5)$$

where $C_1=0.0833$ for $L_2/L_1 \gg 2$,

q is the distributed load over the surface, which in this case is equal to the pressure difference across the plate.

L_1 and L_2 are the smaller and larger dimensions of the plate (rectangle).

The maximum deflection at the center of the plate (window), w_{max} is:

$$w_{max} = \frac{C_2 q L_1^4}{E h_p^3}, \quad (4.6)$$

where $C_2=0.0285$ for $L_2/L_1 \gg 2$,
 E is Young's modulus,
 h_p is thickness of plate (window).

The resulting moments and deflections are shown in table 4.3. Note that the coefficients in equations 4.5 and 4.6 are valid for Poisson ratio of 0.3. The Poisson ratio for the acrylic is 0.37 and for the PPG starphire glass is 0.22.

	glass window	side acrylic windows	top/bottom window
q [kPa]	100	100	100
L_1 [in] ([m])	6 (0.15)	6 (0.15)	3.5 (0.09)
E [Pa]	6×10^{10}	3.3×10^9	3.3×10^9
h_p [in] ([m])	0.75 (0.019)	1.5 (0.038)	1.5 (0.038)
w_{max} [μm]	3.71	8.42	0.98
$(M_x)_{max}$ [N]	193	193	66

Table 4.3: Bending strength and center-point displacement for glass and acrylic windows.

Using Solid Works, simulations were performed for the bending of the windows (Fig.4.3). The results are shown in table 4.4. The values for the deflections obtained from the simulations differ by factors of about 2 and 7 from the theoretical values. This can be explained by the fact that for the theoretical calculations, it was assumed that the windows are rectangular plates, clamped at all 4 sides, while the real shapes of the windows are different (especially for the acrylic windows). Also, the boundary conditions in the simulations were different and were closer to the real scenario. The deflections obtained from the simulations are satisfactory (they are in the micrometer range) and should not hinder optical measurements⁴. Based on the maximum stress values obtained from the simulations, the factors of safety for both the glass and the acrylic are larger than 10: $FS_w > 10$.

	glass window	top acrylic window
w_{max} - maximum deflection [μm]	6.90	6.95
σ_{max} - maximum stress [Pa]	3.36×10^6	4.41×10^6

Table 4.4: Windows bending and shear (Solid Works simulations).

⁴Note that in the final design, the width of the top/bottom acrylic windows is 3 inches, which would result in lower bending stress and lower deflection. Also, the waviness of both glass and acrylic is larger than the maximum deflection.

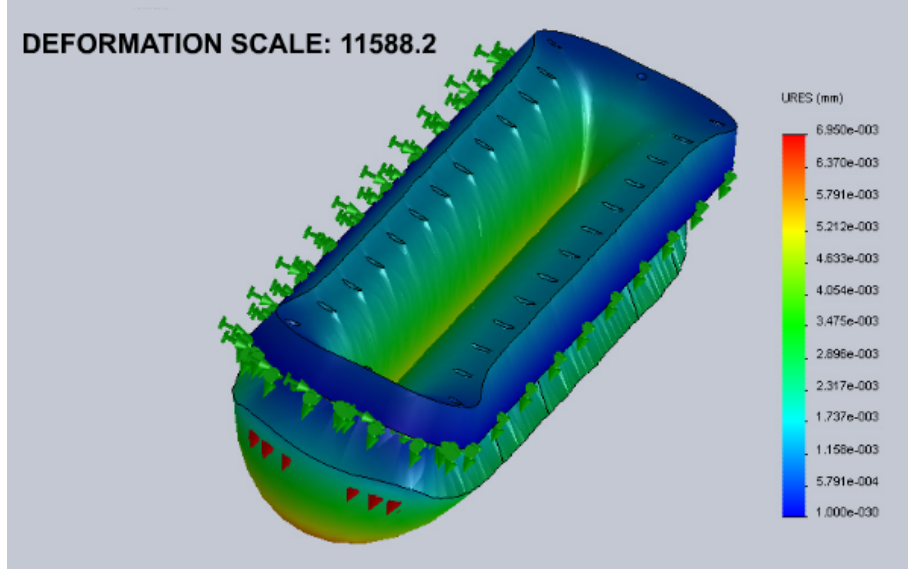


Figure 4.3: Solid Works simulation for deflection of top/bottom window. The green arrows represent fixed surfaces

4.6 Fasteners

When the tunnel is pressurized, a force will be acting on the windows, as a result of the higher pressure on the inside of the test section. As the windows are kept in place by the fasteners, the threads of the fasteners will experience shear stress. The thread shear area for one fastener was found using:

$$A_f = \frac{\pi}{2}(d_f - 0.064952/n_f)l_f, \quad (4.7)$$

where A_f is the shear area,
 d_f is the diameter of the fastener,
 n_f is the number of threads (per inch), and
 l_f is the contact length.

Note that the tolerance of the thickness of the windows and retainers was not accounted for. Without accounting for the uneven distribution of the stress, the total shear area A_{tsa} is:

$$A_{tsa} = A_f N_f, \quad (4.8)$$

where N_f is the number of fasteners.

The shear stress on the fasteners σ_f is calculated using equation 4.9 and is shown in table 4.5.

$$\sigma_f = F/A_{tsa}. \quad (4.9)$$

where F is the force acting on the window (in normal direction)

	large acrylic window	large glass window	small window
N_f	28	28	30
d_f [in]	0.25	0.25	0.25
n_f [1/in]	20	20	20
l_f [in]	0.17	0.30	0.17
A_f [in ²] ([mm ²])	0.066 (42.6)	0.116 (74.8)	0.066 (42.6)
A_{tsa} [in ²] ([mm ²])	1.845 (1190)	3.256 (2100)	1.977 (1275)
F [kN]	12.259	12.259	7.419
σ_f [kPa]	10300	5957	5819

Table 4.5: Stress on fasteners. The uneven distribution of the load on the fasteners was not accounted for. Also, by using slightly longer fasteners for the acrylic side windows, the stress on this set of fasteners could be decreased by 75%. In case the thickness of the side acrylic window is $.75+.03''$ (the maximum allowable thickness according to the drawings), the contact length will be decreased, increasing the load on the fasteners by 20%.

The axial stress on the bolts is calculated using:

$$\sigma_{fa} = F / \left(\frac{\pi d_f^2}{4} \right). \quad (4.10)$$

The maximum axial stress on the fasteners is 13824 kPa (for the large windows) which is larger than the shear stress.

The smallest factor of safety for the fasteners is FS_f :

$$FS_f = \sigma_y / \sigma_{fa}, \quad (4.11)$$

where σ_y is the yield stress of steel ≈ 200 MPa.

Thus $FS_f \approx 15$.

4.7 Welds

Based on [14], the stress at the weld σ_w is:

$$\sigma_w = F_w / A_w, \quad (4.12)$$

where F_w is the force on the weld,
and A_w is the throat area of the weld.

Due to the difference in pressure between the outside and inside of the test section, the force acting normal to the throat area F_p will be:

$$F_p = \sqrt{2} F_{px}, \quad (4.13)$$

where F_{px} is the force of pressure acting in a horizontal direction (Fig.4.4).

$$F_{px} = \Delta p L_{TS} a_{TS} / 2, \quad (4.14)$$

where $\Delta p = 100$ kPa is the pressure difference,

$L_{TS} = 36$ inches (0.91 m) is the length of the test section inner surface,

and $a_{TS} = 6$ inches (0.15 m) is the height (also width) of the test section inner surface.

Using equations 4.13 and 4.14, we find that:

$$F_p = 9853 \text{ N.}$$

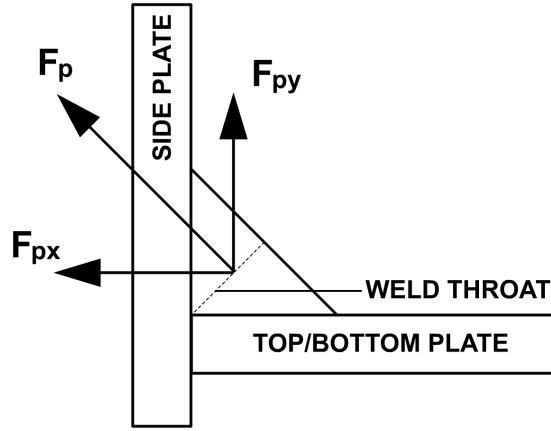


Figure 4.4: Sketch of weld between side plates and top/bottom plates

The force from the weight of the side plate, which is supported by the weld, is about two orders of magnitude smaller than the force due to pressure difference, so it can be neglected. Thus from equation 4.12:

$$\sigma_w = 3840 \text{ kPa.}$$

This value is orders of magnitude smaller than the yield strength of the weld, which is similar to the yield strength of the steel.

According to [9], the available strength in a weld is R_n/Ω , where $\Omega = 2$, and:

$$R_n = 0.6F_{EXX}D_w l_w \sqrt{2}/2, \quad (4.15)$$

where $F_{EXX} = 70 \text{ ksi}$ (3.84 GPa).

D_w is the weld size (in inches)

and l_w is length of the weld

The available strength in one weld (between two plates) is:

$$R_n/\Omega = 5960 \text{ kN,}$$

which is much larger than the expected magnitude of the forces acting on the weld.

4.8 O-Ring Grooves

The nominal values for O-ring grooves (according to the AS568 Standard) were obtained from [11]. Also the following relationship was used:

$$squeeze = 100 \frac{w - c}{w}, \quad (4.16)$$

where w is the O-ring width,
and c is the groove depth.

The ratio of the areas of the cross section of the O-ring and the cross section of the groove is:

$$AR = A_o/A_g, \quad (4.17)$$

where A_o is the O-ring cross sectional area:

$$A_o = \pi w^2/4, \quad (4.18)$$

and A_g is the groove cross sectional area:

$$A_g = c g, \quad (4.19)$$

where g is the O-ring groove width.

For sealing purposes in vacuum applications, it is recommended that a higher squeeze value is obtained. According to [11], the O-Ring leak rate decreases significantly when the squeeze is increased to 30% and in case the O-Ring is lubricated with vacuum grease, there would not be a significant improvement if the squeeze was further increased to 50%. Based on these considerations, it was decided that the squeeze would be increased to a minimum of 30% by decreasing the groove depth. The desired groove depth c_d was obtained from the equation:

$$c_d = w - \frac{\text{squeeze}_d w}{100}, \quad (4.20)$$

where squeeze_d is the desired squeeze.

The new Area Ratio AR_d was calculated using:

$$AR_d = 100A_o / (g c_d). \quad (4.21)$$

The following dimensions and tolerances were selected by trial and error method until reasonable tolerances were achieved for the groove depth, while desired squeeze was at least 30% and AR_d was less than 100%.

The values in the table below represent the nominal values for grooves for the various components.

groove nominal values	flanges/side plates		top/bottom plates		retainers	
	for max squeeze	for min squeeze	for max squeeze	for min squeeze	for max squeeze	for min squeeze
w [in]	0.281	0.269	0.106	0.100	0.143	0.135
c [in]	0.220	0.230	0.072	0.080	0.100	0.110
squeeze [%]	22	14	32	20	30	19
g [in]	0.345	0.355	0.141	0.151	0.190	0.200
AR [%]	82	70	87	65	85	65

Table 4.6: Grooves dimensions (nominal sizes)

The following modifications would be required for a range of desired squeeze between 30% and 35% for the flanges and side plates, between 30% and 40% for the top/bottom plates and between 30% and 38% for the retainers.

groove modified values	flanges/side plates		top/bottom plates		retainers	
	for max squeeze	for min squeeze	for max squeeze	for min squeeze	for max squeeze	for min squeeze
squeeze_d [%]	35	30	40	30	38	30
c_d [in]	0.183	0.188	0.064	0.070	0.089	0.095
AR_d [%]	98	85	98	74	95	76

Table 4.7: Grooves dimensions (desired sizes)

With the modified O-ring grooves, the maximum area ratio AR_d is 98% and the minimum squeeze is 30%.

The shear stress on the grooves can be defined by:

$$\sigma_g = p_g c / w_g, \quad (4.22)$$

where p_g is the pressure acting on the groove,

c is the depth of the groove,

and w_g is the distance from the groove to the nearest edge.

The pressure acting on the groove is due to the pressure difference between the two sides of the O-ring and the pressure as a result of squeezing the O-ring. The later is the dominant factor and depending on the hardness of the O-ring, can reach up to 100 pounds per inch of seal [11]. Thus the O-ring closest to an edge will be under the highest stress (the retainer) with a maximum stress of $\sigma_g=1624$ psi (11197 kPa), which is more than an order of magnitude lower than the yield strength of steel.

4.9 Thermal Effects

The coefficients of thermal expansion for PPG starphire glass and 316 stainless steel were obtained from specification sheet for the PPG glass and Solid Works for the steel. The magnitudes of the coefficients are:

$\alpha_g = 9.28 \times 10^{-6} \text{ K}^{-1}$, and

$\alpha_s = 16.0 \times 10^{-6} \text{ K}^{-1}$, respectively.

In the range of $\pm 20^\circ\text{C}$, the maximum difference in elongations will be:

$$\Delta l = (\alpha_s - \alpha_g) l_{wo} \Delta T, \quad (4.23)$$

where l_{wo} is the length of the window opening, and $\Delta T=20\text{K}$.

Thus, $\Delta l = 4.23 \times 10^{-3}$ inches (0.1 mm), which is about one half of the minimum clearance between the glass window and the side plate (0.01 inches or 0.25 mm).

4.10 Contraction and Diffuser Fabrication

The contraction and diffuser/transition components were fabricated at a local shop. They were made out of composite materials, and were built around molds (plugs), which defined their inner shapes. The tolerances on the plugs were ± 0.030 inches. The plug for the transition component had to be collapsible since it wouldn't have been able to slide out of the component, once the component was completed (Fig.4.5). The layup was as follows:

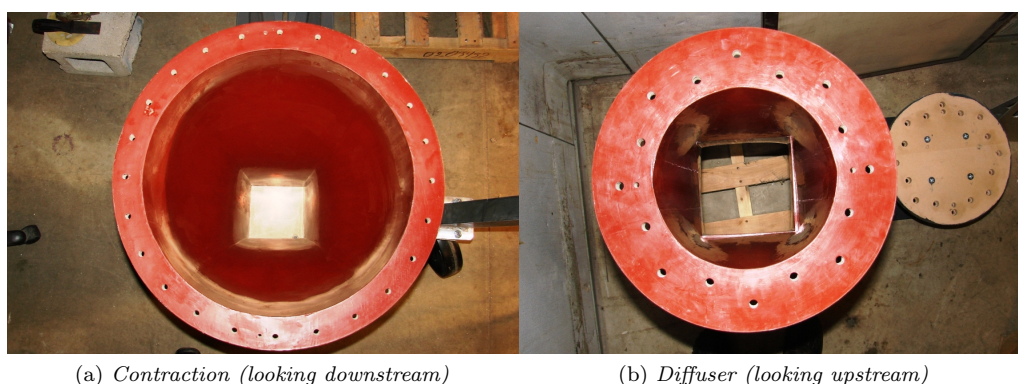
- waxed plugs
- gelcoat
- BimaxTM
- woven roving
- core materials
- woven roving
- BimaxTM
- epoxy laminated resin

The layup was vacuum bagged at 24" Hg for twelve hours. Drill inserts were located in the plug so that flange holes could be accurately drilled prior to demolding. Plywood flanges were routed flush to the plug.

The finished components had only minor imperfections of the inner surface. The flow surface of the diffuser turned out not "perfectly" smooth, since the collapsible plug was made out of more than one section (Fig.4.6). The other imperfections from the fabrication process were a minor mismatch of the inlet/outlet surfaces of the components (Fig.4.7), and a few indents in the outside edge of the flanges (Fig.4.8).



Figure 4.5: *Contraction (left) and diffuser (right). Diffuser is placed on top of the diffuser plug.*



(a) *Contraction (looking downstream)*

(b) *Diffuser (looking upstream)*

Figure 4.6: *Inner surfaces of the contraction and the diffuser*

4.11 Test Section Fabrication

The test section was also fabricated at a local shop. During the manufacturing, a few modifications were made compared to the drawings shown in Appendix C - the welds between the plates were decreased in size to $1/16$ inches (Fig.4.9(a)), and the flanges were welded on both sides of the plates that they were made out of. The additional welds on the flanges were not continuous, since they were used only to straighten the flanges (Fig.4.9(b)). Both of these modifications were made in order to minimize distortions from the desired shape during welding, and as can be seen in section 4.7, they do not affect the overall integrity and strength of the test section. Another modification was made to the acrylic side windows, which were initially designed to fit tightly in the side-plates window openings. Chamfers had to be added on parts of some of the edges, since these edges would have rested on the seam-welds between the side and top/bottom plates otherwise (Fig.4.9(c)).

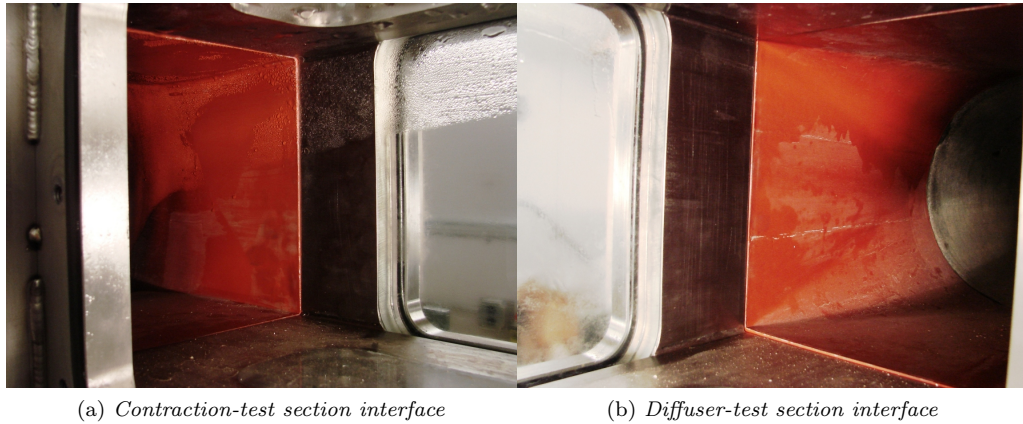


Figure 4.7: Contraction and diffuser interfaces with test section. In (b), the interface between the transition/diffuser and the round diffuser can be seen as well.



Figure 4.8: Indents on the sides of the contraction and diffuser flanges. In (a) an indent in the outside edge of the contraction flange is shown. This was the only indent through which water was leaking after the tunnel was initially filled. The leak stopped after the O-ring between the flanges was replaced. In (b) the largest indent is shown (no water was leaking from it).

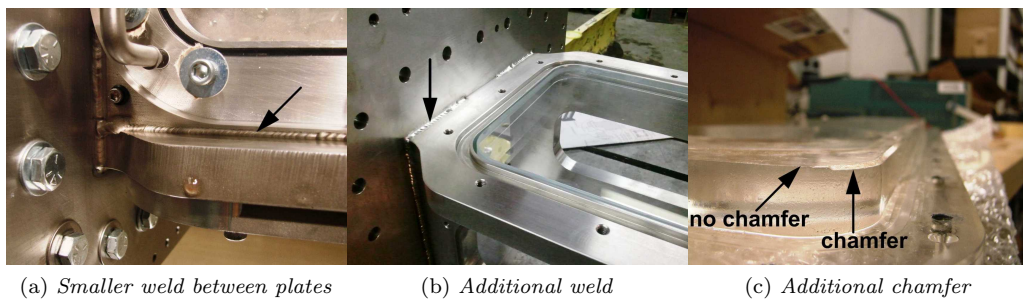


Figure 4.9: Test section modifications. In (a) the actual weld between the bottom and one of the side plates is shown. The weld shown in (b) compensated for the outward curving of the flange. Note that in (c) the chamfer is discontinued and not present at the portion of the edge which is exposed to the flow.

A few imperfections in the test section resulted from the fabrication process. Although extreme care was taken to clamp the parts of the test section as straight as possible before welding them (Fig.4.10), the plates were distorted during the welding. The edges, on which the side windows rest were not perfectly parallel anymore, which meant that the glass windows would not rest flat on

them, but rather rest on the two highest points of these edges and wobble when force was applied at different locations (Fig.4.11(a)). Another imperfection was that these edges were not polished before the test section frame was welded (Fig.4.11(b)). Also, the eight corners of the inner surface of the test section frame were seamed (to avoid water penetrating between the plates), but as a result of that, the shape of these corners was not perfectly square anymore, even after the corners were machined additionally after the test section frame was welded together (Fig.4.11(c)). One last imperfection was the offset between the flange faces (which mate to other flanges) and the faces of the side and top/bottom plates (which are parallel to the flange faces). This imperfection was more noticeable on one side (though not visible) and almost not present on the other side of the test section.



Figure 4.10: Test section parts, clamped together before welding.

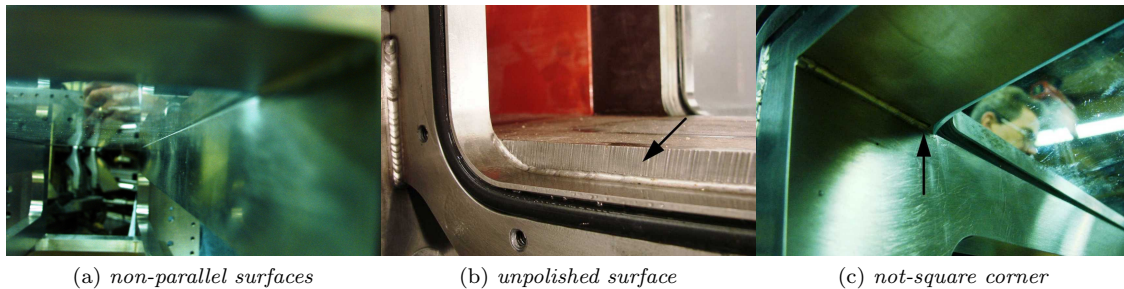


Figure 4.11: Test section imperfections. In (a) the gap between the window and the test section linearly varies with distance (reaching zero at the further end). In (b) the face on which the windows rest is shown (note that it is not polished). In (c) one of the eight corners of the inner surface is shown (note the deviation from square shape, especially in proximity to the window).

Overall, the imperfections that resulted from the fabrication process should not significantly affect the performance of the new test section.

4.12 Installation

Much of the assembly work was performed by UNH Mechanical Engineering undergraduate students. The flow loop from corner 1 to corner 4 had previously been assembled by Scott Hiland, after the parts had been cleaned, and powder coated on the outside. Before the installation of the contraction, test section and diffuser, an additional tunnel base, four additional tunnel supports and a motor base were designed, fabricated, and installed. A new TECO Westinghouse DHP0202 motor and ABB ACS800-U31 drive were purchased and installed as well (Fig.4.12).

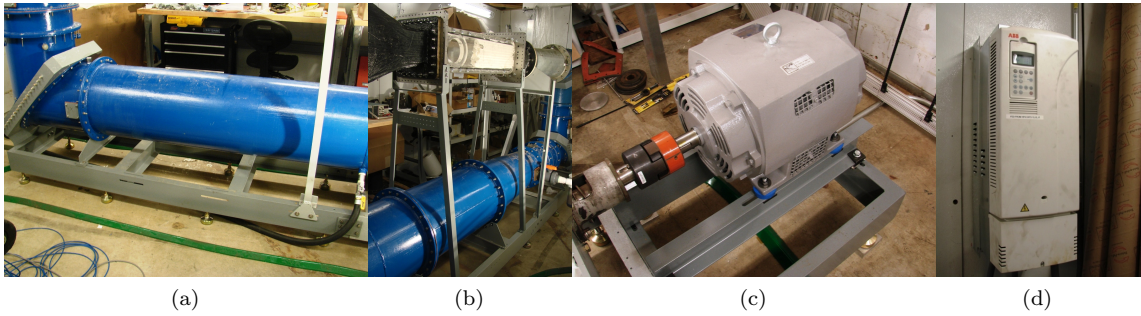


Figure 4.12: *Water tunnel upgrades. In (a) - new supports and tunnel base (attached to the old base via connecting plates); (b) - test section supports; (c) motor, coupling and motor support; (d) drive.*

The remainder of the installation between corners 4 and 1 was undertaken as follows: First, the round diffuser (part 2), the small diffuser (part 1), the test section (part 0), the contraction (part 25) and the small straight duct (part 22) were installed (c.f. Fig.1.3). Thus, the required length for part 24 (straight duct) could be measured more precisely (Fig.4.13(a)). Then, the contraction and test section were disassembled. An available straight duct from the previous flow loop was shortened to become part 24, and it was attached to the honeycomb (part 23) before the two parts were installed. Since the honeycomb was extending beyond the flange of part 23 (c.f. Fig.1.4), force was required to mate parts 23 and 24. The honeycomb was positioned vertically on the ground, and the short duct (part 24) was lowered and pressed towards the honeycomb, guided by long bolts (Fig.4.13(b)). Before the fasteners were tightened, the mating flanges were cleaned off of derbies and O-ring sealant was applied. The two parts were then installed. It was noted however that the upper leg was tilted to one side, so it was necessary to rotate the section between parts 18 and 24 and install smaller bolts at the interface between parts 17 and 18 (Fig.4.13(c)). After the portion of the upper leg was straightened, the contraction was installed.

The test section could fit in the space between the contraction and diffuser if a moderate force was applied (if no O-rings were installed on the flanges), however in order to simplify the installation with proper sealing, a car jack and a long rod were used to slightly spread the contraction and diffuser supports apart.

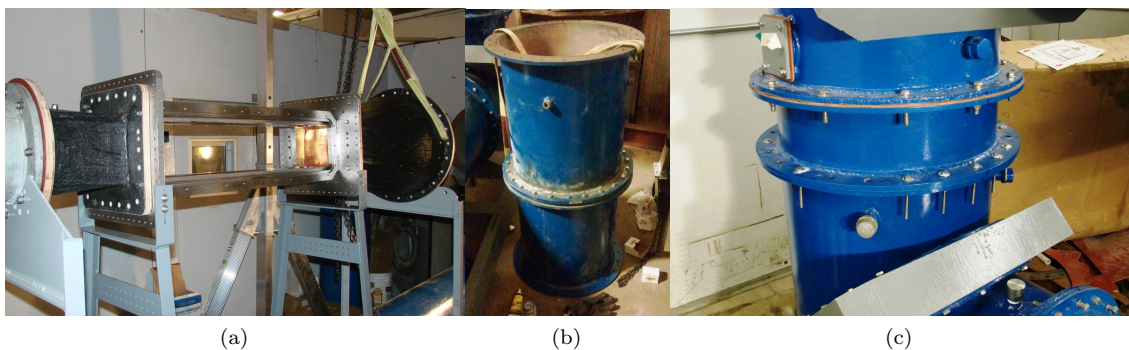


Figure 4.13: *Installation of water tunnel components. In (a) - diffuser, test section and contraction installed, to accurately measure the required length for part 24; (b) - assembly of part 23 - the honeycomb and part 24; (c) - interface between parts 17 and 18 with smaller bolts, after the upper leg section was rotated.*

After all major components were assembled, the windows had to be installed. The bottom and top windows were installed first, since they fit much more tightly than the other windows and it is harder to install them. For the installation of the glass windows, first, O-ring sealant was applied to the surfaces on which the glass would rest. Then, the glass was put and held in place, while

the retainer was placed on top of it. After making sure that both O-rings were not displaced, the retainer was tightened.

After filling the tunnel, water seemed to have penetrated through the retainer O-ring on one side. It was later discovered that a small piece of the glass window had broken off⁵, which was thought to have happened during installation. Although the glass windows have a chamfer, it seemed that the glass window was resting on the weld between the bottom plate and the side plate, rather than on the side faces of the top and bottom plates.

Other upgrades and modifications to the tunnel and the surrounding area include (Fig. 4.14): spill berm placed around the tunnel to manage leaked water; filter system; and new electrical wiring of the room (see Appendix B for schematics of the wiring). A lift/drag balance was designed by UNH senior students Ben Comtois, Ryan Therrien, and Spencer Roux as a TECH 797 Ocean Projects capstone project. Also, three hydrofoil sections were machined - NACA 0015, NACA 63-424, and a bidirectional version of the NACA 63-424 (Fig.4.15). The foils can be easily attached to the force balance, which fits through a circular opening in one of the acrylic side windows [17]. A DEKKER RVL020W vacuum pump connected to a 60 gallon vacuum tank and a pressurized air line were connected to the tunnel. Solenoid valves were installed to control the pressure in the test section independently of the velocity.

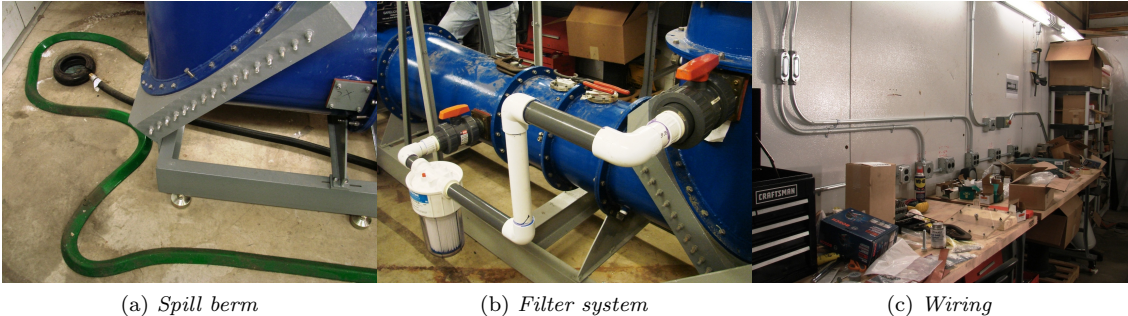


Figure 4.14: Additional water tunnel upgrades

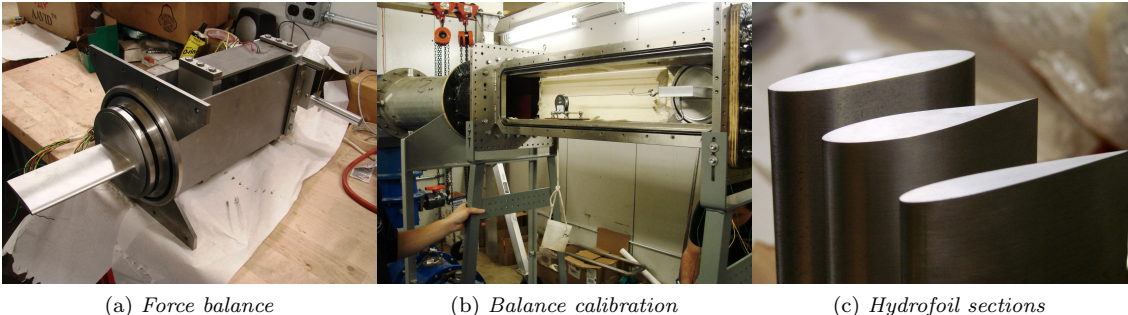


Figure 4.15: Force balance and hydrofoil sections

A rendering of the tunnel in Solid Works and a picture of the assembled tunnel can be seen in Fig.4.16 and Fig.4.17.

⁵The chipped part of the window is covered by the retainer and the window remains usable. After it was reinstalled, no water was penetrating out of the test section (as a result of the damage)



Figure 4.16: *Assembled tunnel – Solid Works rendering*



Figure 4.17: *Assembled tunnel – picture of the tunnel*

4.13 Suggestions for Design and Installation

It was very useful to machine the last conduit component (shortening of the straight 18-inch-diameter pipe) after all other components were completed, since it was machined very precisely and that simplified installation significantly. It would have been beneficial to machine the high-precision components (like the test section) after the less accurately machined components were fabricated (the contraction and diffuser). In this way the mismatch of the components inlets/outlets could have been further minimized.

It is rather easy to operate the renovated tunnel. In case there is a need to disassemble components, it is recommended that the test section is removed first and installed last, since these assembling/disassembling procedures seemed to be the simplest. In case the test section does not slide out of place easily, it is recommended to cut the flange O-rings and pull them out. When installing the test section, the larger gap (the offset between the flanges and the sides of the plates discussed in Section 4.11) should be facing downstream.

Installation of windows is fast and simple and can be performed by one or preferably two people. If O-rings are not present, it is suggested that they are put in place and O-ring/vacuum grease sealant is applied so that they remain in place while the window is installed. This procedure is also valid for the bottom window – the O-ring sealant should prevent the O-ring from falling. Special care should be taken for the glass window, in order to avoid breaking it on the weld (Section 4.12). Before installing the window, it is recommended to apply sealant on the surfaces at which it will rest. Also, it can be tightened slightly, and in case there are leaks after the tunnel is filled, it can be tightened further until the leaks are eliminated.

5 Experimental Results

The water tunnel was calibrated using several experimental techniques:

- Particle Tracking Velocimetry (PTV)
- Laser Doppler Velocimetry (LDV)
- Particle Image Velocimetry (PIV)
- Differential Pressure Measurements (between the inlet and outlet of the contraction)

5.1 PTV measurements

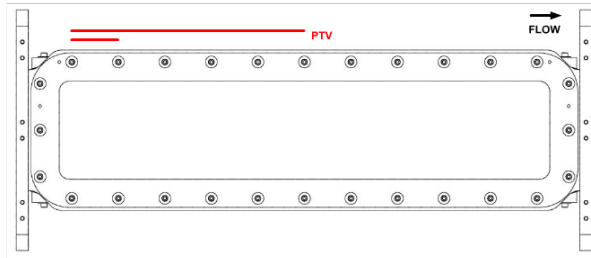


Figure 5.1: *PTV measurements location*

it was more convenient to use the locations of centers of bolts for scale. A ruler was placed on the screen, connecting the centers of bolts located at the same stream-wise direction. Videos were played and/or watched frame by frame, and particles were tracked as they were passing the first, second and last visible set of bolts (Fig.5.3).

PTV measurements were performed at motor speeds, ranging from 180 rpm to 1260 rpm. The field of view of the high speed camera was approximately half of the test section (from its inlet to its middle - Fig.5.1). Videos were recorded at each motor speed setting. For lower speeds the injected $11\ \mu\text{m}$ particles were tracked, but at higher speeds, air was entrained in the test section so the air bubbles were tracked instead (Fig.5.2). Although pictures for scaling were taken before and after the experiment,

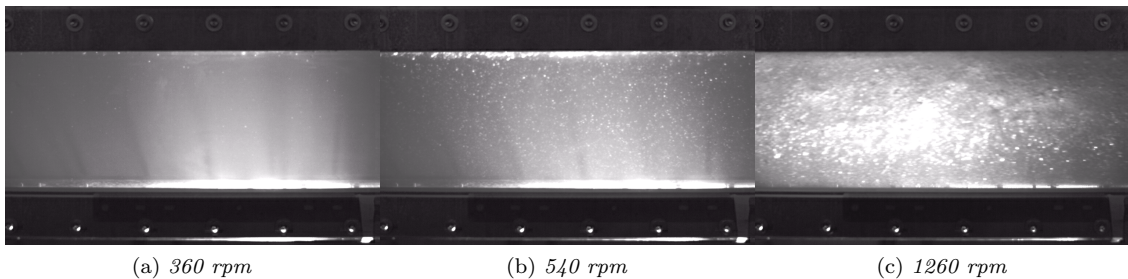


Figure 5.2: *Snapshots of flow in the test section at different motor speed settings. Note that air started to be entrained in the flow at around 540 rpm. At approximately this speed, the pressure in the test section becomes lower than atmospheric pressure.*

The frame numbers at which these events happened were recorded for three particles for each speed setting. The actual distances that the particles passed were larger than the distances between the center of bolts (which are respectively 2.91 inches and 14.52 inches). By applying Snell's law we can estimate the actual distance that particles travelled if we know how far they were from the wall (Fig.5.4). However, since the light was not from a laser (spot lights were used), the particles could have been anywhere along the width of the test section.

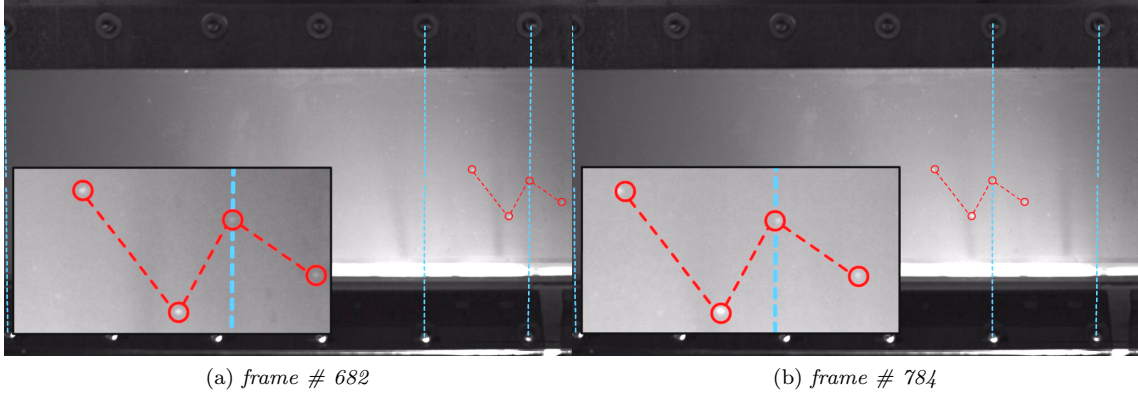


Figure 5.3: Sample frames from PTV measurements for motor speed of 300 rpm. Note that the relative displacement (in pixels) between different particles has changed between the two frames - this is partially due to the camera angle.

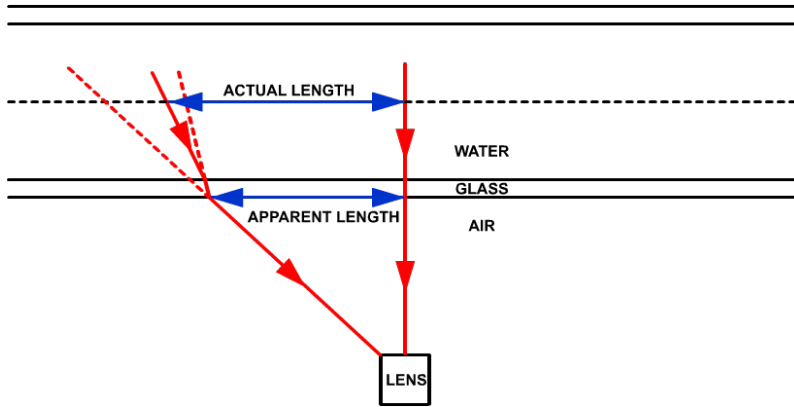


Figure 5.4: Schematics of light paths for the PTV experiment (top view)

For the calculations, the minimum possible distances (L) were used (as if particles were very close to the glass). This resulted in under-prediction of the actual velocities. The number of frames (n_{fr}) required for the particles to pass the distance between the first two sets of bolts (2.91 inches) and between the first and the last sets of bolts (14.52 inches) was computed. Based on the frame rate and the known distances, the corresponding average velocities (V_{av}) were computed from:

$$V_{av} = \frac{L}{n_{fr}/fps}, \quad (5.1)$$

where fps is the frames per second and $fps = 3600$ fps.

As expected, the relationship between the motor speed ω and the test section speed \mathbf{V} is linear (Fig. 5.5). If there are no limitations at higher motor speed settings (such as cavitation at the impeller), the value for the maximum test section speed should be higher than originally planned, since the new motor is capable of reaching 1780 rpm instead of 1500 rpm [16]. Also, the flow rate at a given motor speed is slightly higher than that of the original tunnel, which might be due to decreased energy losses throughout the circuit [12].

Apart from being used for a calibration plot, the PTV data were used to obtain qualitative results. As it was seen in Fig.5.3, groups of particles could be tracked, and there did not seem to be significant change in the spacing between the particles at any speed (except for particles close to the top/bottom walls).

Although the exact distance between the particles and the walls (in horizontal direction) could not

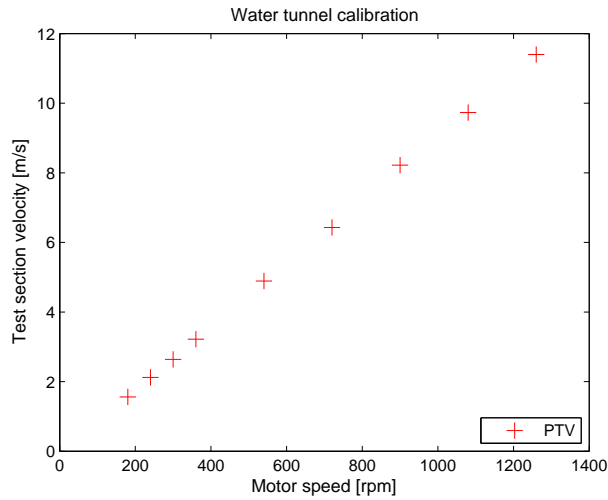


Figure 5.5: *PTV Calibration*

be determined precisely, the vertical proximity of particles to the walls could be observed. For the motor speed setting of 300 rpm, particles close to the (top/bottom) wall were tracked as well¹. It was very clear that the particles closer to the wall are slower. An approximate velocity profile for this speed setting can be seen in Fig.5.6. Particles were tracked as they were passing through the first and last sets of bolts. The distance from the wall was measured relative to the test section height, which is 6 inches.

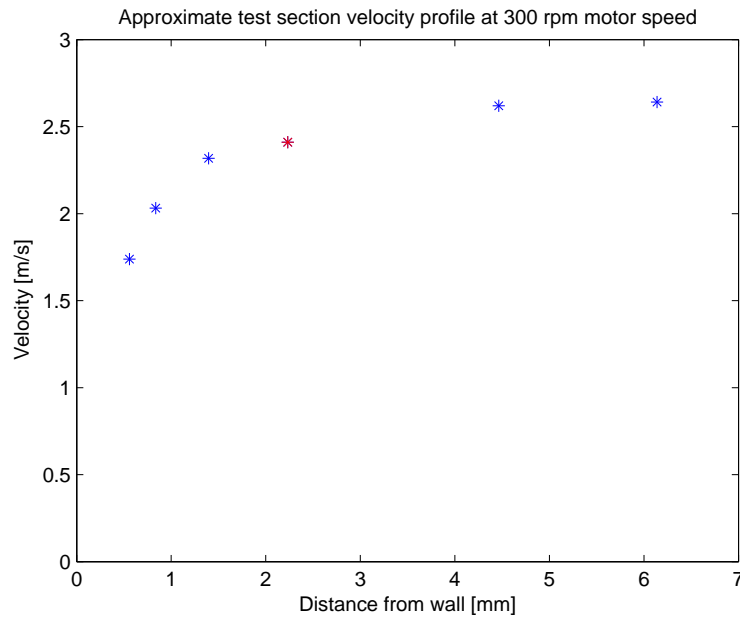


Figure 5.6: *Approximate velocity profile from PTV measurements for motor speed of 300 rpm. Note that the particle that was located 2.4 mm from the wall significantly approached the wall as it moved downstream, hence it must have slowed down.*

¹At this speed setting particles could be tracked most easily.

5.2 Laser Doppler Velocimetry

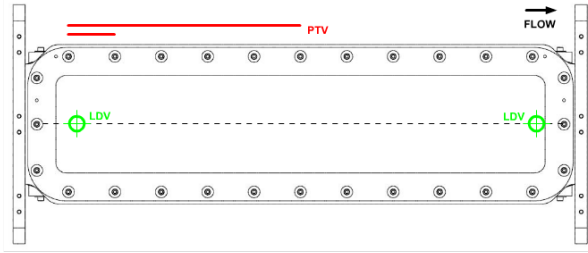


Figure 5.7: *LDV measurements locations*

Laser Doppler Velocimetry measurements were performed at motor speeds ranging from 180 rpm to 1351.8 rpm. Center-point velocity (velocity at the center of the square cross-section) were measured for various speed settings close to the inlet and close to the outlet of the test section (Fig.5.7). 5000 data points were obtained for each speed setting and location. The velocities measured close to the inlet were used for calibration (Fig.5.8). Theoretically, the velocities measured at the center point should

be the highest for a given location in stream-wise direction. As it could be expected, the measured velocities were higher than the ones predicted by the PTV measurements.

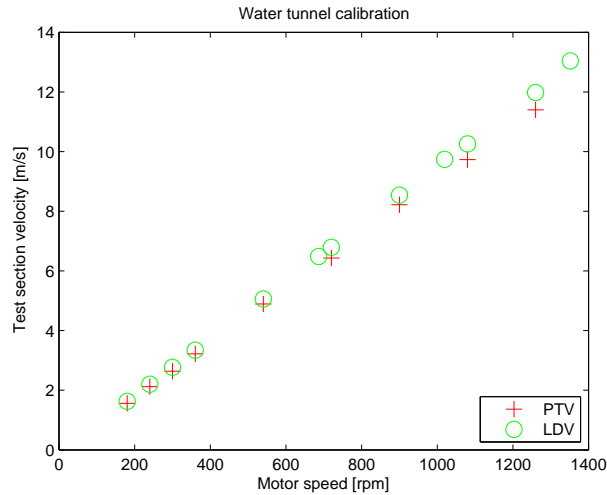


Figure 5.8: *LDV Calibration*

Velocity profiles were obtained (across the width of the tunnel) for the given vertical position (the center of the tunnel) and the given locations downstream. Profiles were obtained for 3 speed settings corresponding to the speeds for which numerical simulations were performed (6.48 m/s, 9.69 m/s, and 12.87 m/s center-point velocity). For each measurement point in space, 1000, 500, and 100 data points were taken for the small, medium and high speed respectively. As expected, the boundary layer grows in downstream direction, and as a result, the center line velocity increases (Fig.5.9). The LDV data agrees well with simulation data for the low speed and confirms that the variation of velocity outside of the boundary layer is well within 1% of the center-line velocity. For the high speed, the measured increase in center-line velocity differs by approximately 1% from the numerically predicted value.

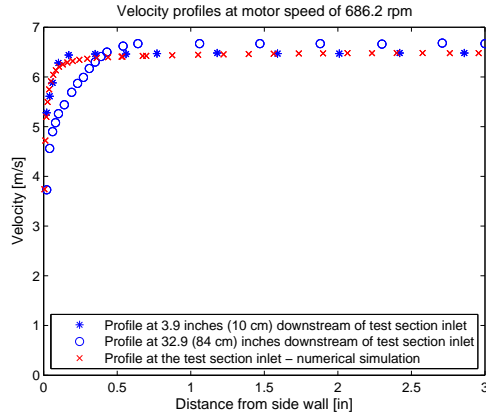


Figure 5.9: LDV profiles and comparison with numerical simulation results

5.3 Particle Image Velocimetry

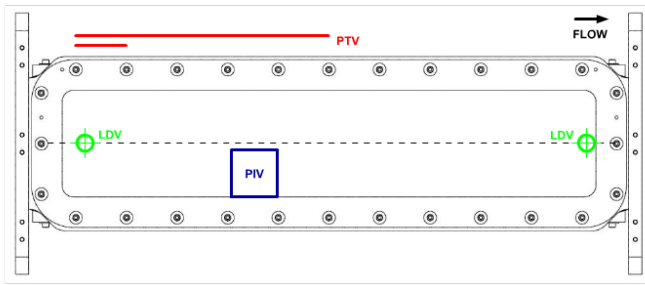


Figure 5.10: PIV measurements locations

Particle Image Velocimetry measurements were performed at motor speeds ranging from 180 rpm to 1351.8 rpm. The field of view was close to the center of the test section in stream-wise direction, encompassing the bottom half of the test section in vertical direction (Fig.5.10). 1000 images were obtained at 3600 fps (or higher). Calibration data points were obtained by averaging the velocities in stream-wise direction (to obtain a profile) and averaging the profile (neglecting the boundary layer) Thus, the averaged velocity would be close to the center-

line velocity, and as it could be expected, the resulting values were larger than the values obtained from the LDV measurements, since the field of view was further downstream of the location for LDV calibration data measurements (Fig.5.11).

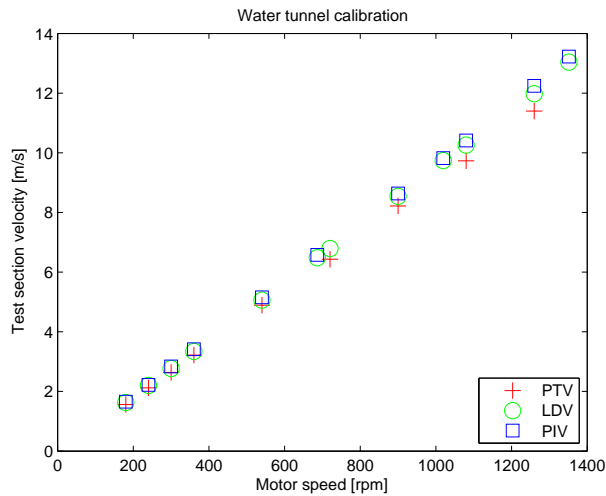


Figure 5.11: PIV Calibration

A sample velocity contour can be seen in Fig.5.12. The velocity increases downstream (positive x-direction) and decreases in direction of the wall (negative y-direction).

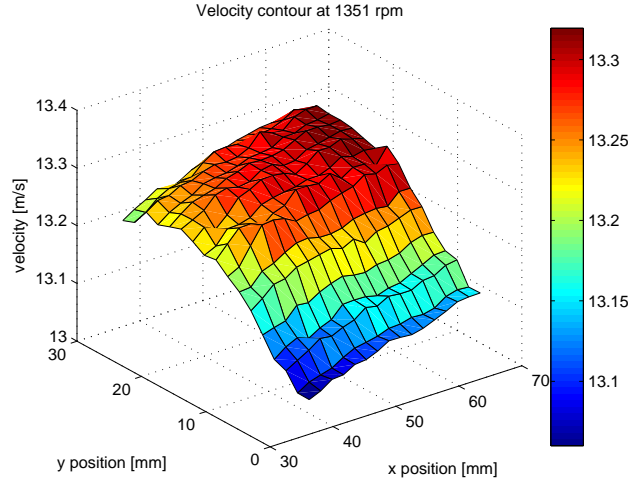


Figure 5.12: *PIV velocity contour at the middle of the test section at approximately 13 m/s test section speed. The boundary layer is not shown completely.*

5.4 Pressure Measurements and Calibration Equation

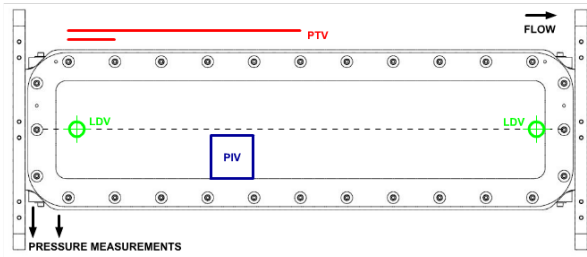


Figure 5.13: *Pressure measurements locations*

Pressure measurements were performed at motor speeds ranging from 180 rpm to 1351.8 rpm. Differential pressure transducers were connected between the straight duct before the test section and the pressure port in the bottom plate at the entrance of the test section (Fig.C.3) and between the duct and the first port in the bottom window (closest to the test section inlet - Fig.C.9). Based on these pressure measurements and the Bernoulli's principle, test section velocities were estimated. As it could

be expected these velocities were lower than the ones obtained from the LDV measurements since the pressure measurements provide information for the average velocity above the test section pressure port, neglecting friction effects (Fig.5.14).

Since the LDV measurements have the smallest inherent error in them, and since a velocity profile was obtained for a position close to the one where most studied object will be placed, water tunnel speed will be estimated from the linear fit to the LDV calibration data (Fig.5.14).

$$\mathbf{V} = 0.00947 \times rpm \text{ m/s} \quad (5.2)$$

where \mathbf{V} in this case is the test section velocity at the center of the tunnel (close to the inlet), and rpm is the motor speed in revolutions per minute.

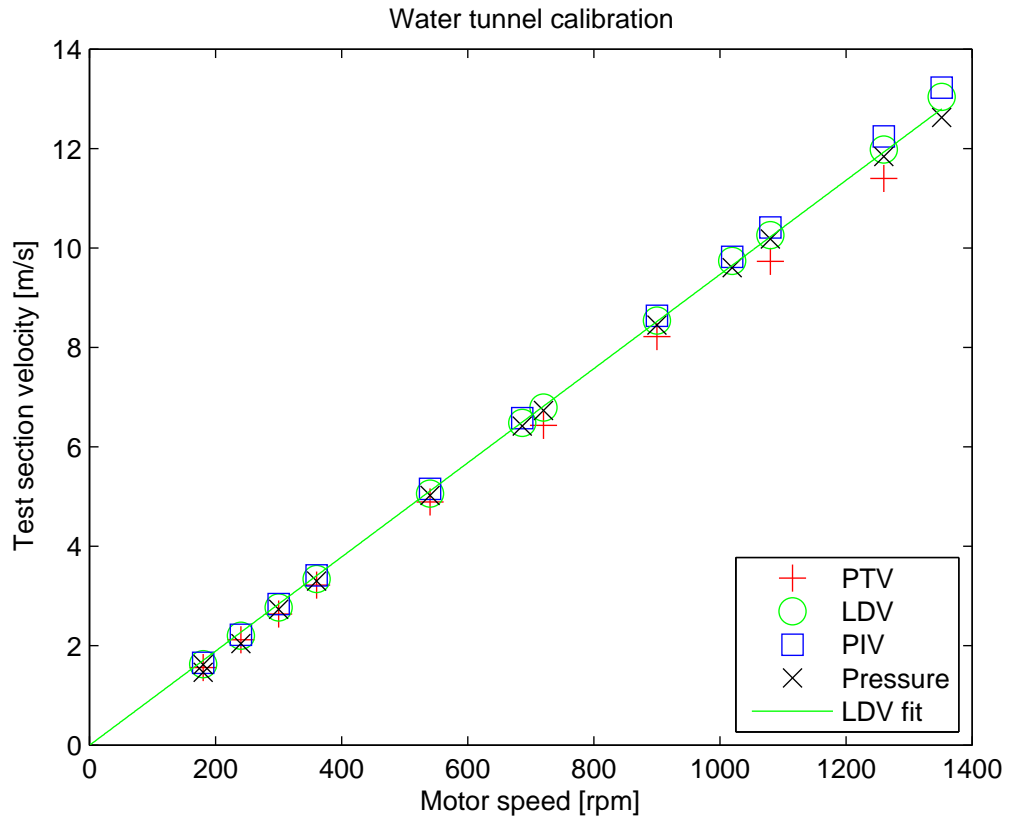


Figure 5.14: *High-speed water tunnel calibration*

During experiments, the motor speed will be set based on the fore-mentioned calibration. The differential pressure between the inlet and outlet of the contraction will be measured in order to monitor speed, and the differential between the test section and atmospheric pressure will be used to monitor test section pressure.

6 Conclusion

A new contraction, test section and diffuser for a high-speed water tunnel were designed, fabricated and installed. The tunnel operated as expected, and there were no leaks from the new components, except for the two minor leaks mentioned in chapters 4.10 and 4.12 which were initially present due to the use of an old O-ring and due to a minor damage on the glass window. PTV, LDV, PIV and pressure measurements were performed and a calibration for the high speed water tunnel was obtained.

The contraction shape is defined by a fifth-order polynomial, has an L/D ratio of 1.5 and a contraction ratio of 7. The test section has a 6 inches \times 6 inches square cross-section with optical access from all four sides, and full optical access through the side-windows (the test section can be rotated by 90° so that the side windows can become top/bottom windows). The transition/diffuser component has a constant increase in the cross-sectional size in downstream direction and has an effective half-angle of 3.5° .

In the design process, it was very beneficial that an excel spreadsheet was used with all design/operation variables (e.g. test section inlet and outlet size, flow rate, tunnel pressure, diffuser effective half-angle, etc.). Thus all other dependent variables could be easily calculated (e.g. test section flow speed, boundary layer growth, blockage, etc.). Another useful tool was the simplified CAD model of the existing and designed parts of the entire tunnel. The model was extremely helpful, especially when the new base and supports were designed.

Different test section designs were considered, but the most simple one, having a square cross-section, seemed to be the best option. Only a few modifications were made to the design during the fabrication process (Sections 4.10 and 4.11). The undersized O-ring grooves allowed for an excellent sealing and did not cause any problems with offsetting the flow surface of the windows in respect to the flow surface defined by the test section frame. The use of the transition as a diffuser was beneficial, since more length was available for the test section and there were no negative consequences on the flow quality. The tunnel was calibrated and is fully operational. It is now part of the UNH Center for Ocean Renewable Energy infrastructure. It will be used for various experiments (including cavitation studies, hydrofoil design studies, lift/drag measurements, etc.) and will be used in some of the graduate level classes offered at the university. More information about the water tunnel (including calculations, simulations, and drawings) is available on the UNH Center for Ocean Renewable Energy server, or can be requested from the author by e-mail.

Bibliography

- [1] Roger E.A. Arndt and Ernst-August Weitendorf. Hydrodynamic considerations in the design of the hydrodynamics and cavitation tunnel (HYKAT) of HSVA. Technical report, St. Anthony Falls Laboratory, 1990.
- [2] J. H. Bell and R. D. Mehta. Contraction design for small low-speed wind tunnels. *NASA STI/Recon Technical Report N*, 89:13753, August 1988.
- [3] C. Borgnakke, Richard Edwin Sonntag, and Gordon J Van Wylen. *Fundamentals of thermodynamics*. Hoboken, NJ : Wiley, 7th edition, 2009.
- [4] L. Davidson. *Fluid mechanics, turbulent flow and turbulence modeling*. Division of Fluid Dynamics Department of Applied Mechanics Chalmers University of Technology Goteborg, Sweden, 2010.
- [5] Fluent Inc. *FLUENT 6.3 Getting Started Guide*, 2006.
- [6] Fluent Inc. *GAMBIT 2.4 Modeling Guide*, 2007.
- [7] Jacob Den Hartog. *Advanced Strength of Materials*. Dover, 1988.
- [8] R. I. Loehrke and H. M. Nagib. Control of free-stream turbulence by means of honeycombs: A balance between suppression and generation. *Journal of Fluids Engineering*, 1976.
- [9] American Institute of Steel Construction Staff. *Steel Construction Manual*. American Institute of Steel Construction, 13th edition, 2005.
- [10] Parametric Technology Corporation. *Getting Started with Pro/ENGINEER® WildfireTM 4.0*.
- [11] Parker Hannifin Corporation, Cleveland, OH. *Parker O-Ring Handbook*, 50th edition, 2007.
- [12] Harry D. Purdy and Lorenz G. Straub. Model experiments for the design of a sixty inch water tunnel. Technical Report 10,11,12,13,14,15, St. Anthony Falls Hydraulic Laboratory University of Minnesota, 1948.
- [13] H. Schlichting and K. Gersten. *Boundary Layer Theory*. Springer-Verlag, 2000.
- [14] Joseph E. Shigley and Charles R. Mische. *Mechanical Engineering Design*. McGraw-Hill, 5th edition, 1989.
- [15] Ed Silberman, Roger Arndt, and Martin Wosnik. The life and times of the six-inch water tunnel. *St. Anthony Falls Laboratory CHANNEL*, page 11, fall 2009.
- [16] Lorenz G. Straub, John F. Ripken, and Reuben M. Olson. The six-inch water tunnel at the st. anthony falls hydraulic laboratory and its experimental use in cavitation design studies. Technical Report 16, series B, University of Minnesota St. Anthony Falls Laboratory, 1955.
- [17] Ryan Therrien, Spencer Roux, and Ben Comtois. Design of a high speed water tunnel force balance & testing of high performance hydrofoils for marine hydrokinetic turbines. Technical report, University of New Hampshire, 2012.
- [18] H. K. Versteeg and W. Malalasekera. *An introduction to computational fluid dynamics. The finite volume method*. Longman Scientific & Technical, 1995.
- [19] J. M. Wetzel and R. E. A. Arndt. Hydrodynamic design considerations for hydroacoustic facilities: Part I - flow quality. *Journal of Fluids Engineering*, 1994.
- [20] Martin Wosnik and Roger Arndt. Testing of a 1:6 scale physical model of the large, low-noise cavitation tunnel (LOCAT). Technical Report 486, St. Anthony Falls Laboratory, 2006.

- A Water Tunnel Sketch**
- B Water Tunnel Room Electric Wiring**
- C Drawings**

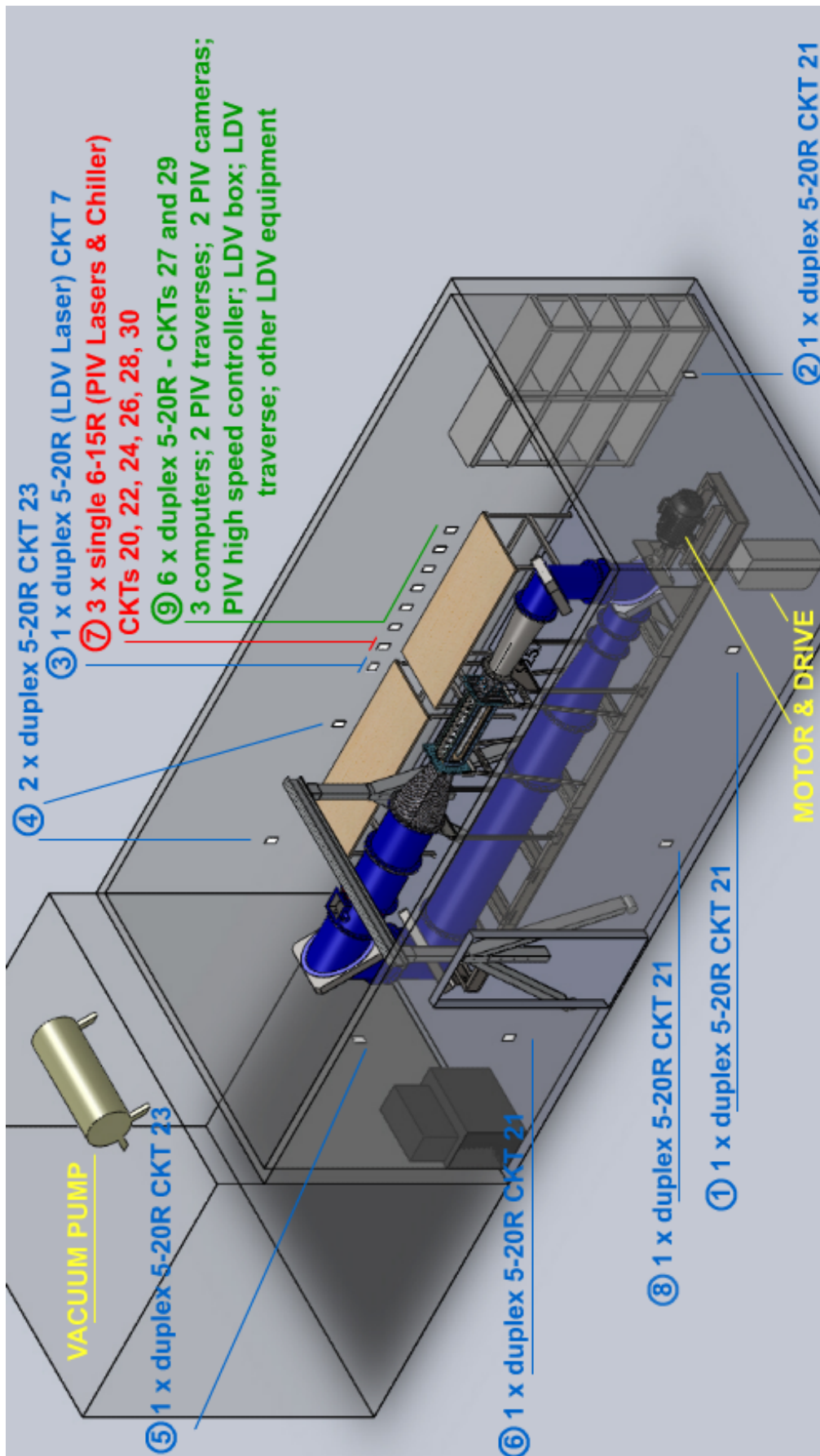
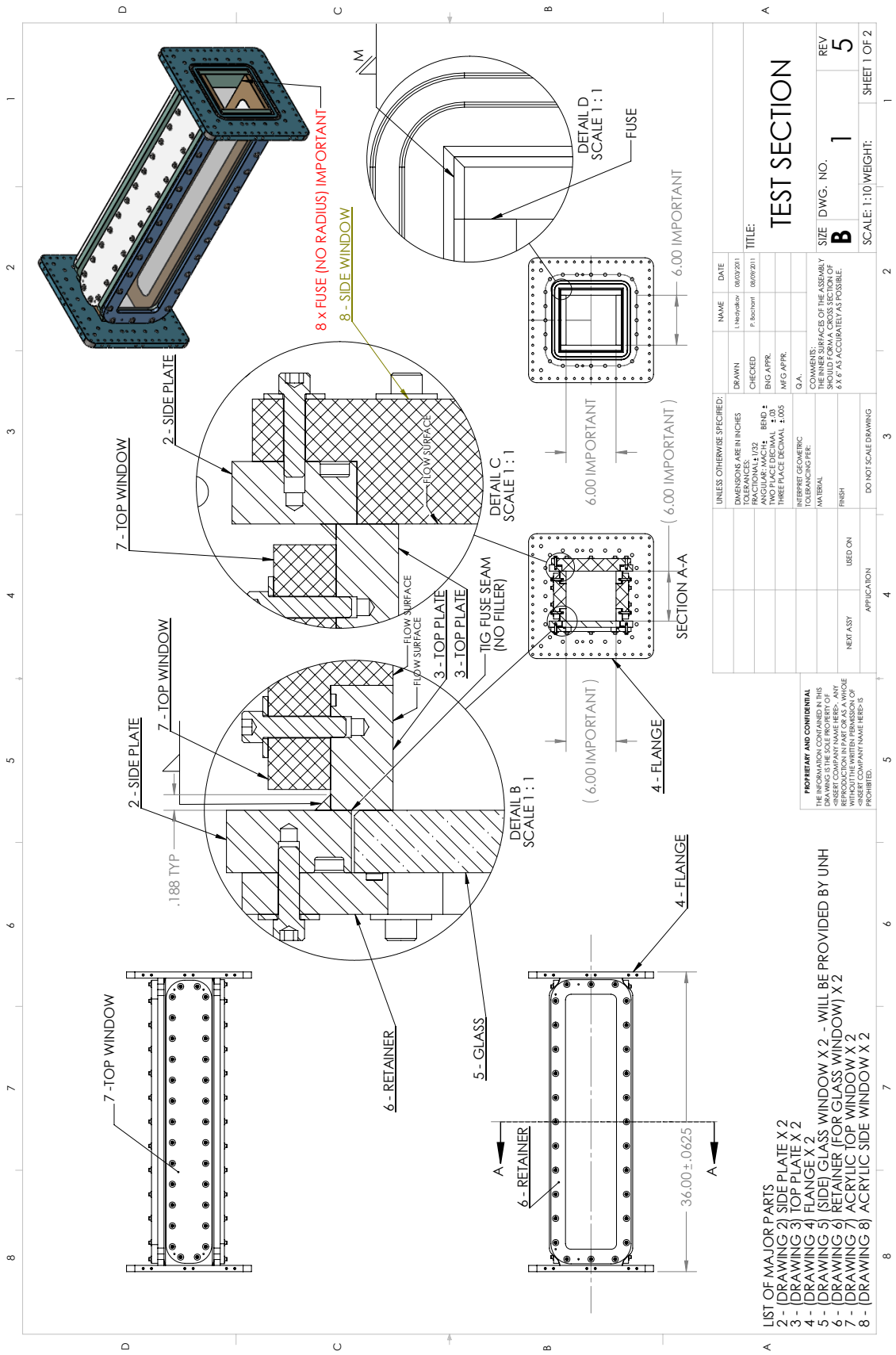


Figure B.1: Water tunnel room electrical wiring. Two light switches controlling the same set of lights are positioned next to the door, and next to the workbenches. Emergency stop for the motor is placed at a convenient location, close to the workbenches.



- LIST OF MAJOR PARTS
 2- (DRAWING 2) SIDE PLATE X 2
 3- (DRAWING 3) TOP PLATE X 2
 4- (DRAWING 4) FLANGE X 2
 5- (DRAWING 5) (SIDE) GLASS WINDOW X 2 - WILL BE PROVIDED BY UNH
 6- (DRAWING 6) RETAINER (FOR GLASS WINDOW) X 2
 7- (DRAWING 7) ACRYLIC TOP WINDOW X 2
 8- (DRAWING 8) ACRYLIC SIDE WINDOW X 2

UNLESS OTHERWISE SPECIFIED:		NAME	DATE
DRAWN	1. Inquiries	P. Bostrom	08/09/2011
CHECKED	FUNCTIONAL 1/32		
ENG APPR.	ANGULAR: MACH: BEND ±		
MFG APPR.	TWO PLACE DECIMAL ±.05		
G.A.	THREE PLACE DECIMAL ±.005		
COMMENTS: SURFACES OF THE ASSEMBLY SHOULD FORM A CROSS SECTION OF 6 X 6 AS ACCURATELY AS POSSIBLE.			
DIMENSIONS ARE IN INCHES		TITLE: TEST SECTION	
FRACTIONAL 1/32		SIZE DWG. NO.	REV
TOLERANCES UNLESS OTHERWISE SPECIFIED:		B	1
FRACTIONAL 1/32		SCALE: 1:10 WEIGHT:	SHEET 1 OF 2
DECIMAL ±.05			
DECIMAL ±.005			
PROPERTY AND CONFIDENTIAL: THE INFORMATION CONTAINED IN THIS DRAWING IS THE SOLE PROPERTY OF UNH. IT IS TO BE USED FOR THE PURPOSES SPECIFIED ONLY AND IS NOT TO BE REPRODUCED OR TRANSMITTED IN ANY FORM OR BY ANY MEANS, WITHOUT THE WRITTEN PERMISSION OF UNH. COMPANY NAME HERE IS PROHIBITED.			
NEST ASY	USED ON	APPLICATION	
FINISH	DO NOT SCALE DRAWING		

Figure C.1: Test section assembly drawing

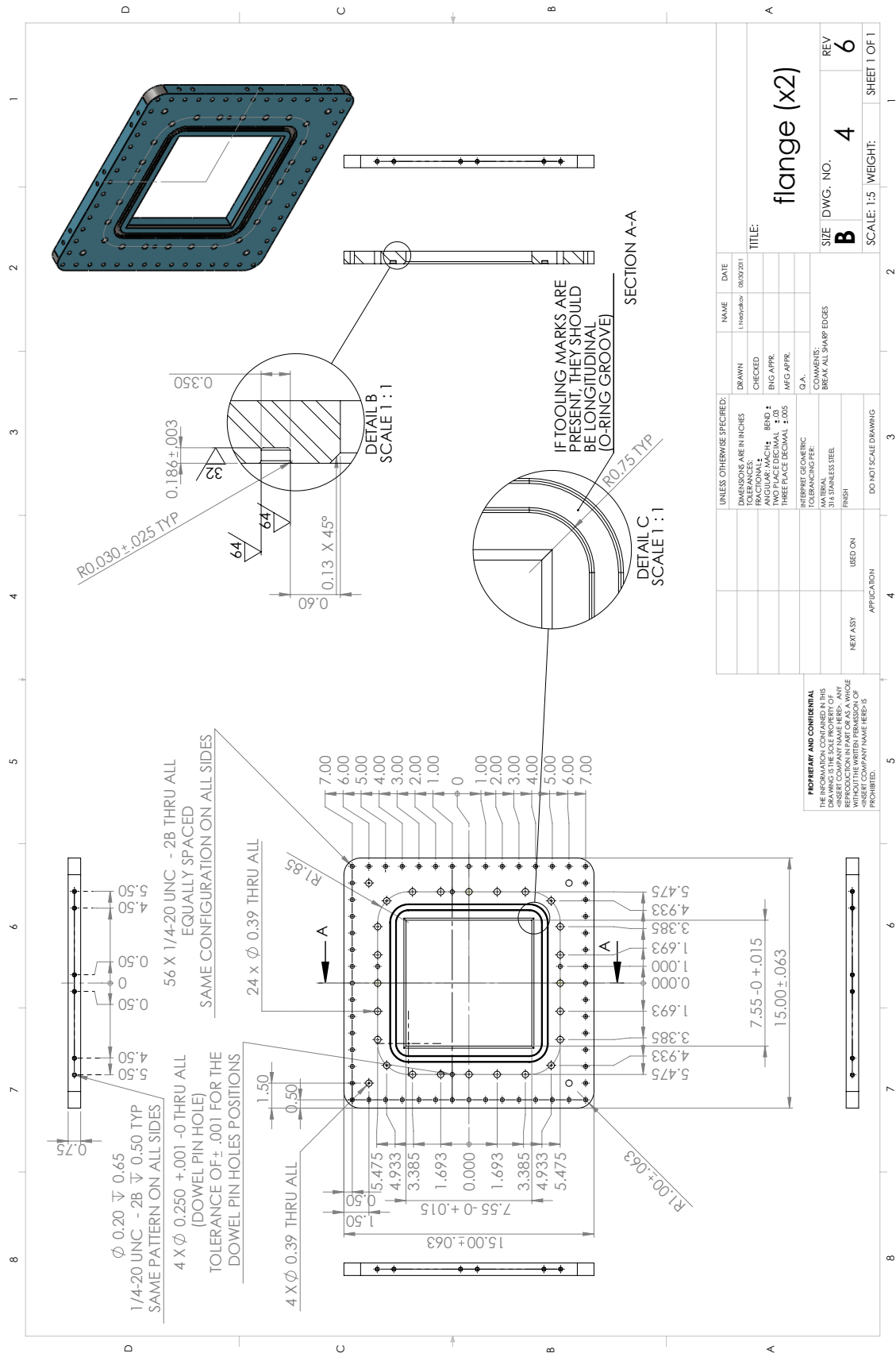
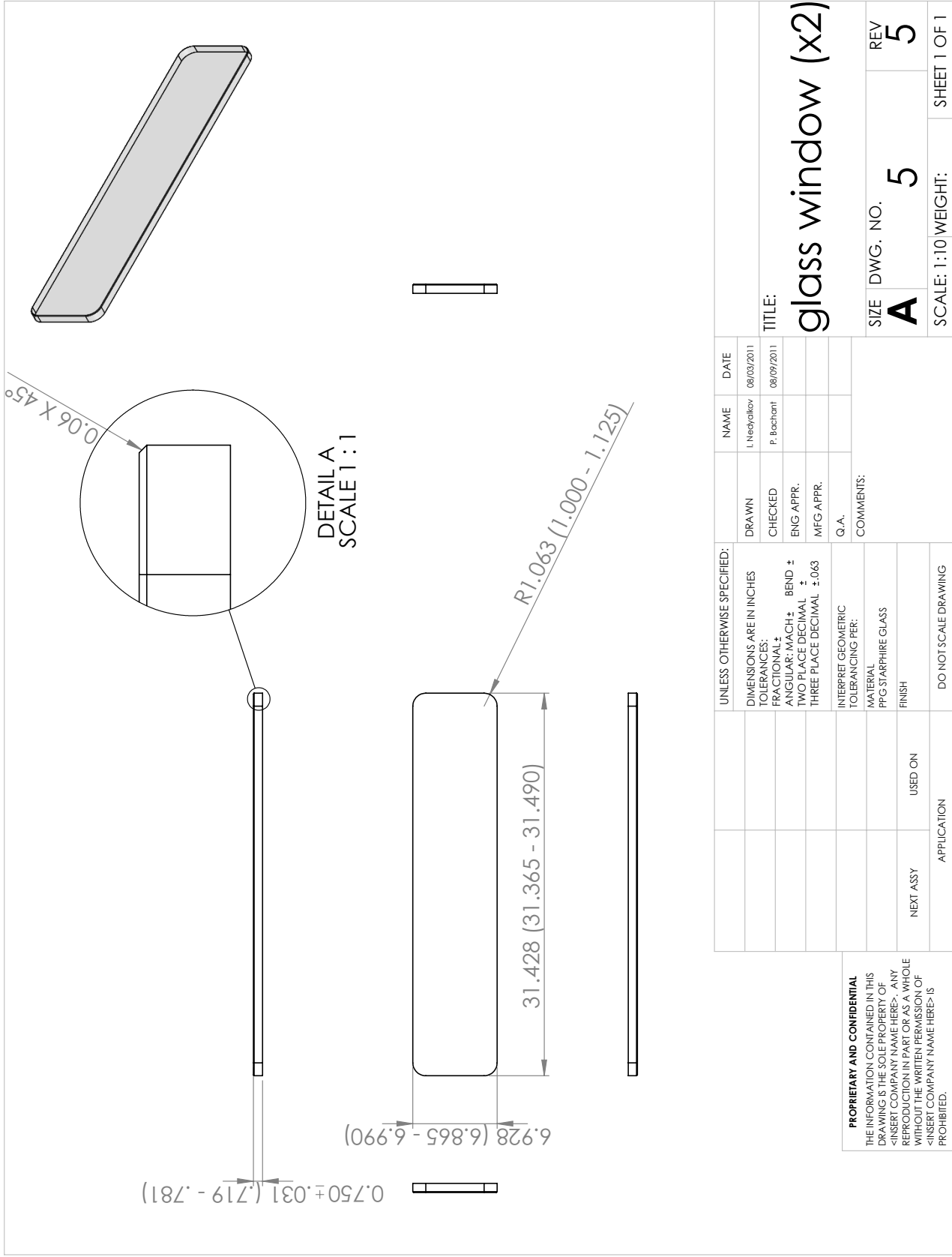


Figure C.4: Flange drawing



PROPRIETARY AND CONFIDENTIAL
 THE INFORMATION CONTAINED IN THIS DRAWING IS THE SOLE PROPERTY OF <INSERT COMPANY NAME HERE>. ANY REPRODUCTION IN PART OR AS A WHOLE WITHOUT THE WRITTEN PERMISSION OF <INSERT COMPANY NAME HERE> IS PROHIBITED.

UNLESS OTHERWISE SPECIFIED:	DRAWN	NAME	DATE
DIMENSIONS ARE IN INCHES	I. Neelyakov		08/03/2011
TOLERANCES:			
FRACTIONAL ±		P. Bochert	08/09/2011
ANGULAR: MACH ± BEND ±			
TWO PLACE DECIMAL ±			
THREE PLACE DECIMAL ±.063			
INTERPRET GEOMETRIC TOLERANCING PER:			
MATERIAL:			
PPG STARPHIRE GLASS			
FINISH:			
USED ON:			
APPLICATION:			
DO NOT SCALE DRAWING			

Figure C.5: Glass window drawing

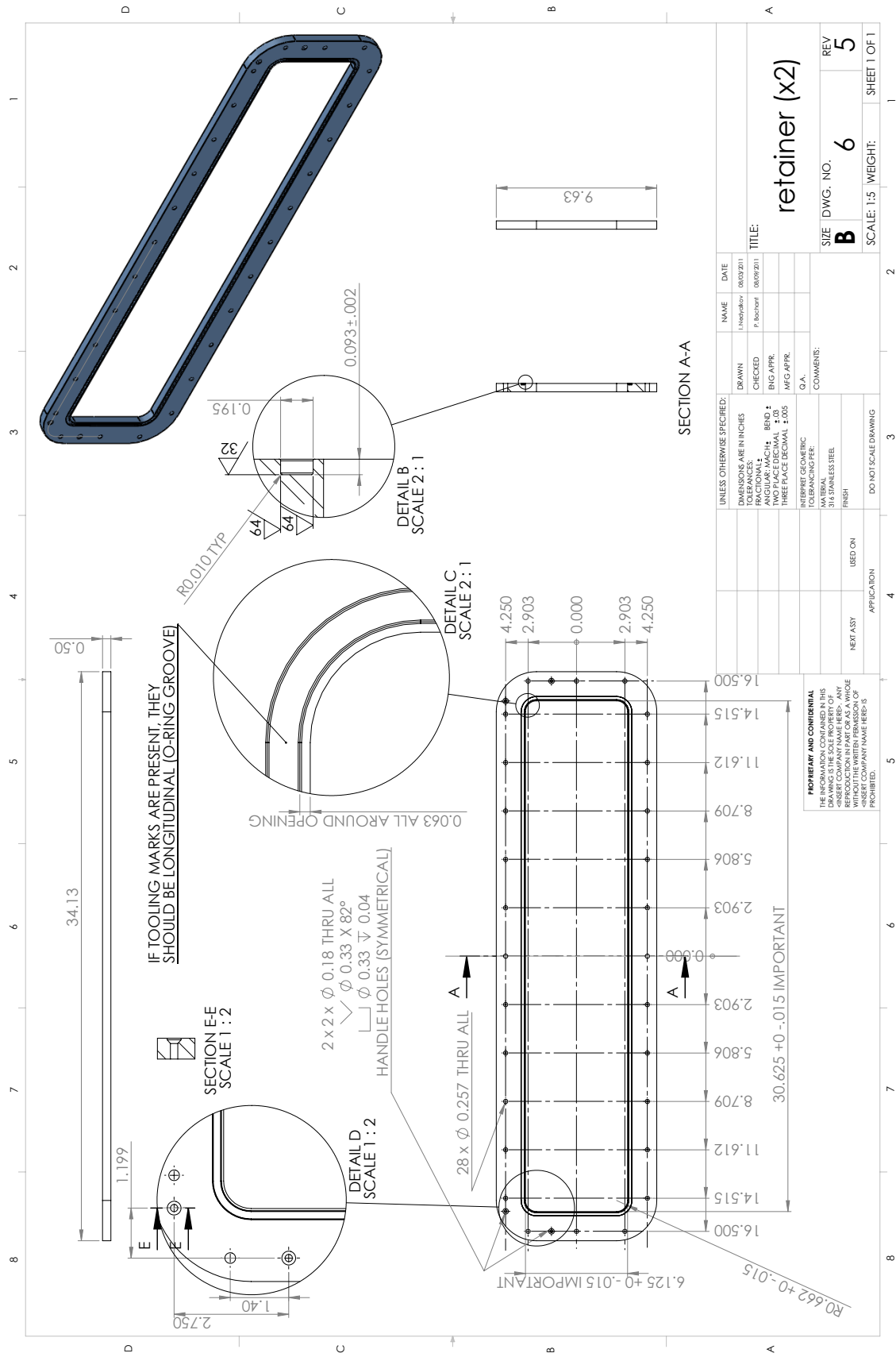
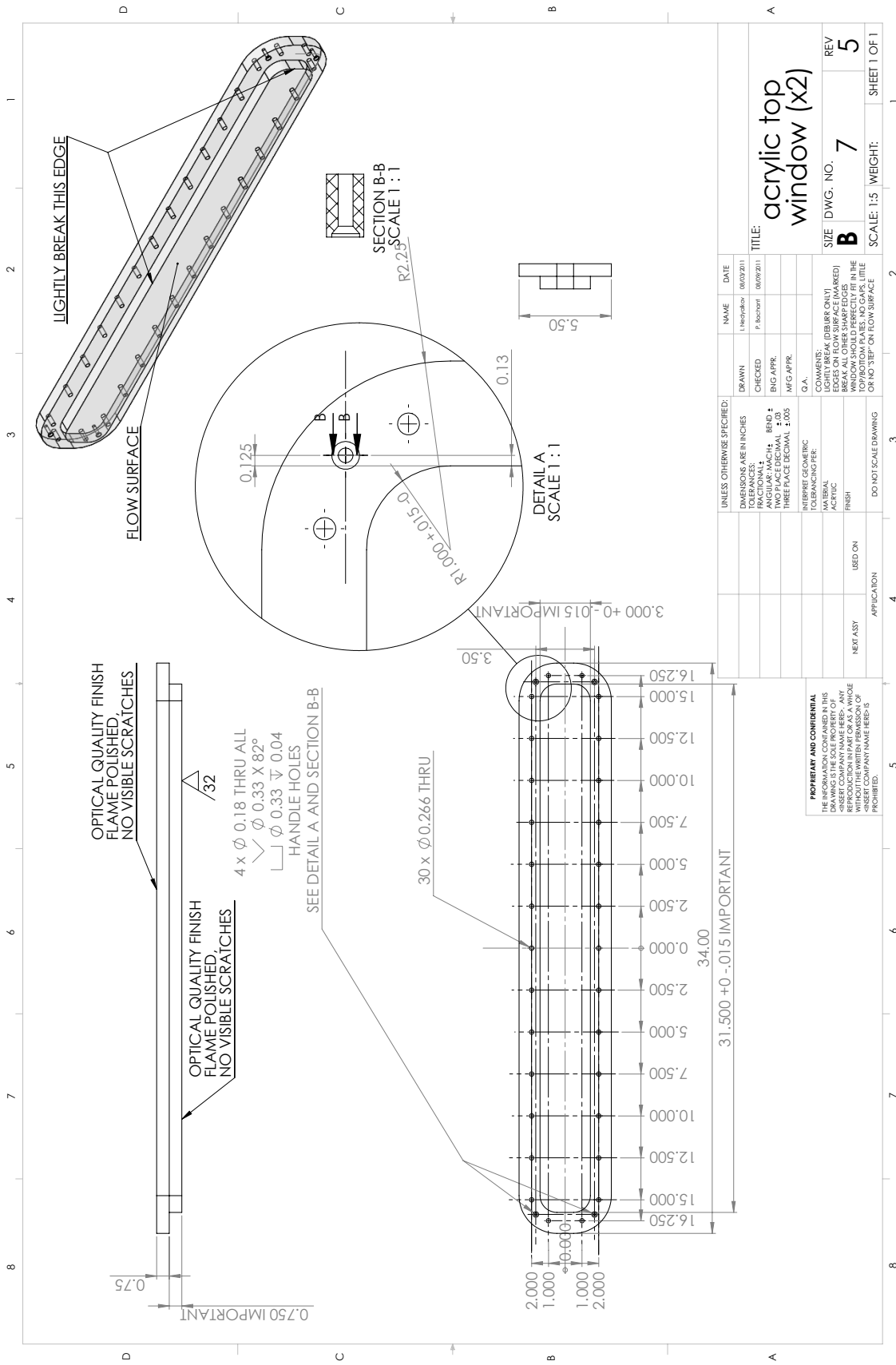


Figure C.6: Retainer drawing



UNLESS OTHERWISE SPECIFIED:	DRAWN	NAME	DATE
DIMENSIONS ARE IN INCHES	1. Hryndokov	08/09/2011	
FRACTIONAL	CHECKED	P. Bachtini	08/09/2011
ANGULAR: MACH: BEND:	ENG APPR.		
TWO PLACE DECIMAL \pm 0.05	MFG APPR.		
THREE PLACE DECIMAL \pm 0.05	G.A.		
INTERPRET GEOMETRIC TOLERANCES:	COMMENTS: (SEE BARS ONLY)		
ACRYLIC MATERIAL	EDGES ON FLOW SURFACE (MARKED)		
FINISH	BREAK ALL OTHER SHARP EDGES		
USED ON	TOP SURFACE		
APPLICATION	OR NO STEP ON FLOW SURFACE		
DO NOT SCALE DRAWING			

PROPRIETARY AND CONFIDENTIAL	
THE INFORMATION CONTAINED IN THIS DRAWING IS THE SOLE PROPERTY OF PERSSON COMPANY. IT IS TO BE USED ONLY FOR THE SPECIFIC COMPANY PART NUMBER AND WITHOUT THE WRITTEN PERMISSION OF PERSSON COMPANY. NAME HERE- IS PROHIBITED.	
NEXT ASY	USED ON
APPLICATION	DO NOT SCALE DRAWING
SCALE: 1:5	WEIGHT:
SIZE DWG. NO. 7	REV 5
TITLE: acrylic top window (x2)	
SHEET 1 OF 1	

Figure C.7: Acrylic top/bottom window drawing (no pressure holes)

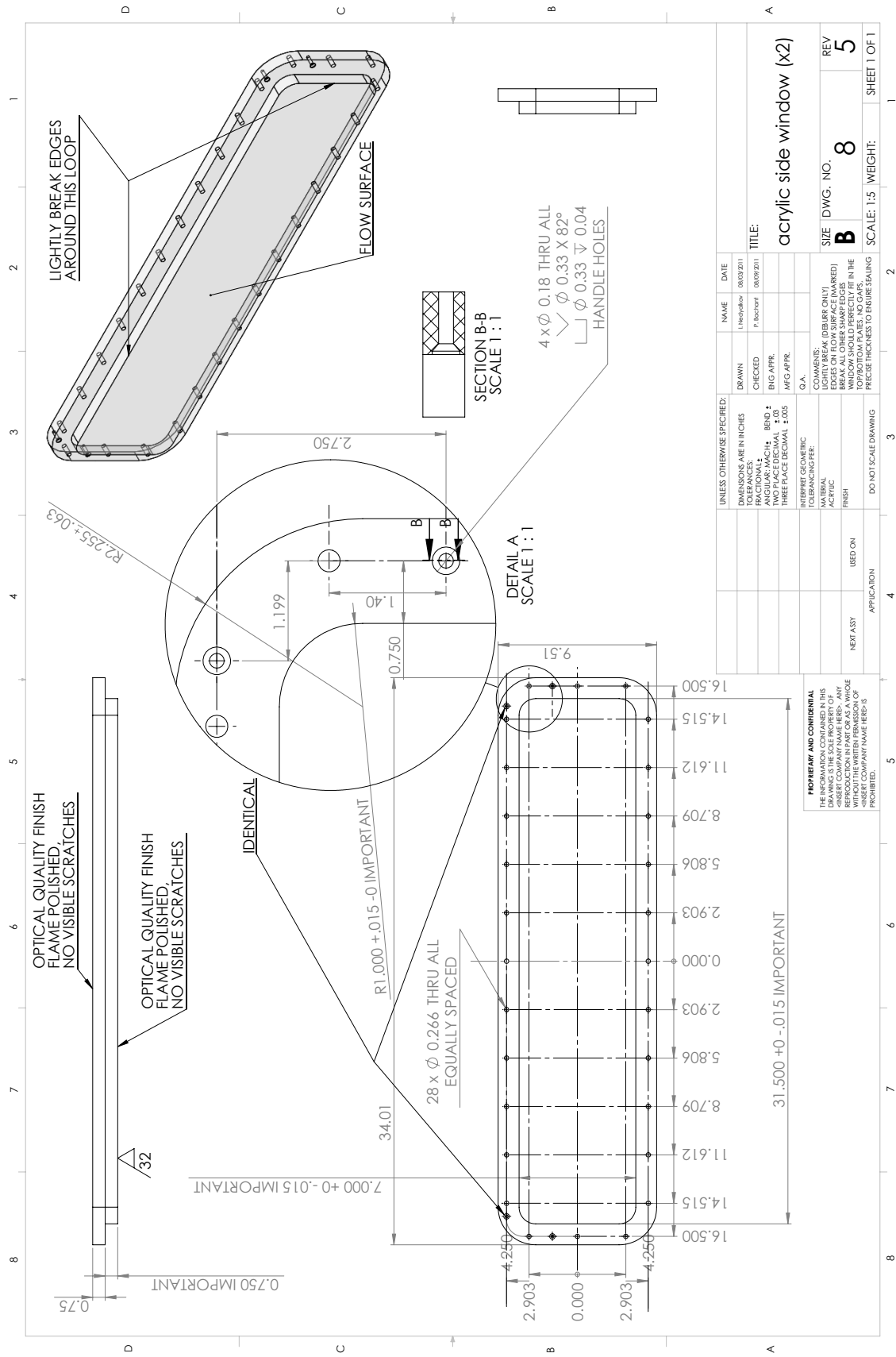


Figure C.8: Acrylic side window drawing

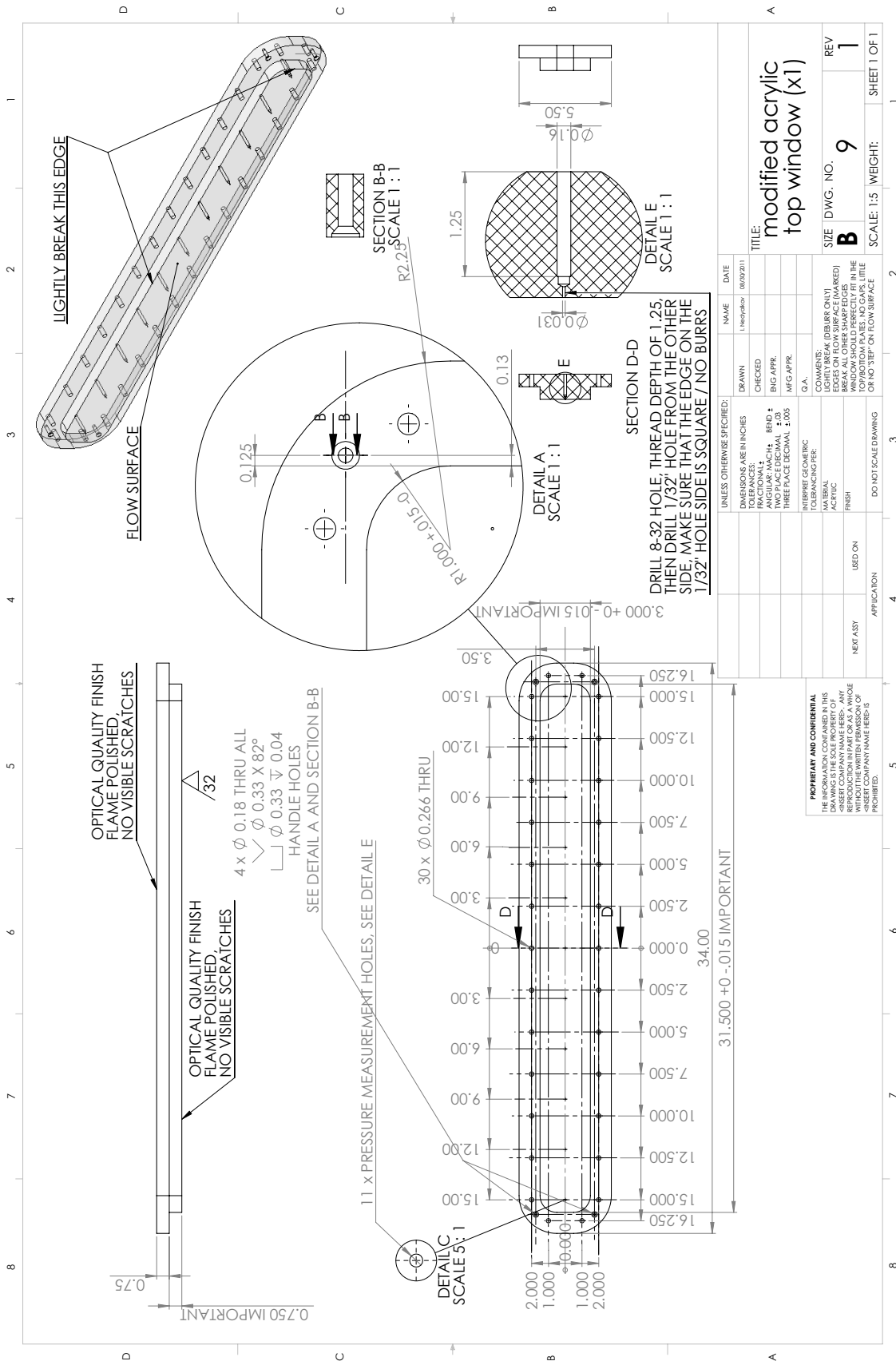


Figure C.9: Acrylic top/bottom window drawing (pressure holes modification)